VILNIUS UNIVERSITY

Life Sciences Center

Institute of Biosciences

Master of Science in Neurobiology, 2nd year student

Kornelija Vitkutė

Master thesis

Intrinsic firing properties and synaptic activity of mouse hippocampal pyramidal neurons during postnatal development

Department of Neurobiology and Biophysics

Supervisor: dr. Urtė Neniškytė

Advisor: prof. dr. Aidas Alaburda

Vilnius 2020

CONTENTS

ABBREVIATIONS

aCSF – artificial cerebrospinal fluid

AMPA – α-amino-3-hydroxy-5-methyl-4-isoxazolepropionic acid

AMPAR – α-amino-3-hydroxy-5-methyl-4-isoxazolepropionic acid receptor

AP – action potential

AR – androgen receptor

CA – cornu ammonis

DG – dentate gyrus

EPSP – excitatory postsynaptic potential

ERß – estrogen receptor ß

ERα – estrogen receptor α

GABA – γ-aminobutyric acid

HEC – hippocampal-entorhinal cortex

HEPES – 4-(2-hydroxyethyl)-1-piperazineethanesulfonic acid

ISI – interspike interval

LTP – long term potentiation

mEPSC – miniature excitatory postsynaptic current

NMDA – N-Methyl-D-aspartate

NMDAR - N-Methyl-D-aspartate receptor

NMDG – N-Methyl-D-glucamine

PSD – postsynaptic density

q – quantal size

R_{in} – input resistance

RT – room temperature

SEM – standard error of mean

sEPSC – spontaneous excitatory postsynaptic current

TTX – tetrodotoxin

INTRODUCTION

Neonatal pyramidal neurons possess immature characteristics that are transformed substantially during the first weeks of postnatal development. Due to the expression and incorporation of mature ion channels and receptors spontaneous activity of juvenile neurons evolves to achieve distinctive and cell-type specific information processing (Moody and Bosma, 2005). Concurrently, neurons branch out and form abundant new synaptic contacts that are sequentially reorganized and refined to form characteristic neural pathways. Faulty pruning of the synapses is often associated with various neurodevelopmental disorders, including autism spectrum disorders and schizophrenia (Neniskyte and Gross, 2017).

To date, a multitude of anatomical, immunohistochemical and imaging studies have provided considerable knowledge about the maturation of neural circuitry. However, such studies should be interpreted with caution, as the structural correlates might not necessarily represent functional properties of the circuitry. For example, morphologically identified synapses might lack pre- or postsynaptic elements that enable efficient synaptic transmission and thus might be functionally silent (Kerchner and Nicoll, 2008). A number of factors that shape mature neuronal networks, such as quantal size, functional synaptic connectivity and strength as well as quantity and functional state of receptors and active firing properties can only be evaluated by direct electrophysiological recordings in living neurons. Unfortunately, most developmental electrophysiological studies evaluate either only synaptic development or only neuronal firing development, without considering how these phenomena shape one another to reach neuronal maturity.

Hippocampus offers an accessible experimental set-up for electrophysiological measurements and has been favored for studying the mechanisms underlying synaptic transmission and plasticity. Additionally, the emergence of genetically engineered mice has offered novel tools to study developmental mechanisms in the brain. However, consistent electrophysiological studies describing the synaptic or neuronal development of hippocampal and cortical pyramidal neurons have predominantly been performed in rats (Albert Y. Hsia et al., 1998; McCormick and Prince, 1987; I Spigelman et al., 1992; Zhang, 2004). Research has shown substantial variations in anatomy and electrophysiology of hippocampal CA1 pyramidal neurons between rats and mice (Routh et al., 2009).

To address some of these discrepancies and to get a better insight to the underlying principles of developing brain, we examined the maturation of hippocampal CA1 pyramidal neurons in mice, characterizing both intrinsic firing properties and synaptic transmission throughout the postnatal development.

AIM AND OBJECTIVES

Aim: To evaluate the postnatal development of intrinsic firing properties and synaptic activity of hippocampal pyramidal CA1 neurons in mice employing electrophysiological techniques.

Objectives:

1. To implement and to optimize a method for the preparation, maintenance, and reliable electrophysiological recordings of acute mouse brain slices, suitable for different stages of postnatal development.
2. To evaluate synaptic activity in hippocampal pyramidal CA1 neurons by characterizing spontaneous and miniature excitatory postsynaptic currents from P5 to P22.
3. To evaluate intrinsic neuronal properties and action potential parameters in hippocampal CA1 pyramidal neurons from P5 to P22.

LITERATURE REVIEW

1.1. Hippocampus as a model to study development

The hippocampus is one of the central brain structures, belonging to the limbic system. It is thought to be involved in the consolidation of short- and long-term memories, as well as to play a role in spatial memory, navigation and even to be associated with regulation of emotions. A relatively simple local circuitry and experimental accessibility has made it one of the most favored brain structures among the electrophysiologists.

In 1966, a Norwegian scientist Terje Lomo was the first one to observe long-term potentiation (LTP) while researching the role of hippocampus in short-term memory in rabbits (Lømo, 1966). While stimulating the neurons of the performant pathway he noticed that neurons responded with stronger excitatory postsynaptic potentials (EPSPs) after applying high frequency stimuli (Bliss and Lomo, 1973). Since then, hippocampus has received a lot more attention, especially in regards of synaptic transmission, plasticity and the developmental mechanisms that shape these phenomena.

1.1.1. The trisynaptic circuit

The hippocampal formation is a highly structured region of the brain, which is organized in a laminar fashion and includes the dentate gyrus (DG), the hippocampus proper and the adjacent parahippocampal cortices. The trisynaptic circuit is considered to be mostly unidirectional and organized in a near-transverse lamella or band across the septotemporal axis of the hippocampus. It contains three main types of excitatory neurons: DG granule cells as well as CA3 and CA1 pyramidal neurons. Neurons from the superficial layers of the entorhinal cortex relay major cortical inputs to the hippocampus, most projections reaching the DG through the performant path. In turn, DG granule cells project their axons (mossy fibers) to CA3 pyramidal cells. These CA3 neurons form recurrent synapses onto other CA3 neurons and project axons (Schaffer collaterals) to the CA1 region, where they synapse onto the dendritic arbors of CA1 pyramidal cells. These CA1 neurons convey the main output of the hippocampus proper back to the deep layers of entorhinal cortex, closing the trisynaptic circuit (Figure 1).

Originally, it was believed that the trisynaptic circuit was fully contained within the transverse lamella of the hippocampus and could represent a functionally independent unit. However, anatomical tracing

studies have revealed an extensive longitudinal distribution of intrinsic hippocampal pathways (Amaral and Witter, 1989). Modern RNAseq technologies show intricate molecular heterogeneity and distinct gene expression domains across different subregions of the mouse hippocampal formation. For example, CA3 has nine different subregions along the longitudinal axis while the traditional CA1 is divided to dorsal, intermediate and ventral domains (Fanselow and Dong, 2010). Recent studies are combining modern gene mapping and anatomical connectivity techniques to refine and shape a much more complex view of a multiscale organization of mouse hippocampal circuitry (Figure 2) and function, where smaller interconnected subnetworks are a part of larger intra- and extra- hippocampal networks (Bienkowski et al., 2018).
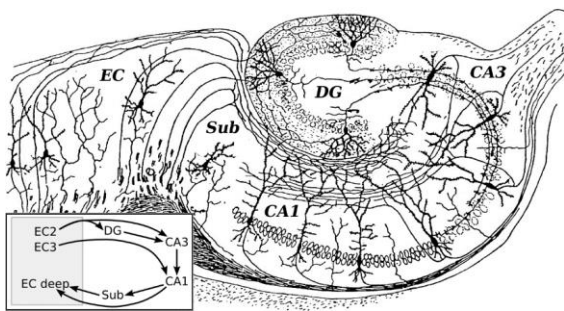
Figure 1 **Modified version of an original 1911 Cajal drawing of hippocampal circuitry**. EC – entorhinal cortex, Sub – subiculum, DG – Dentate gyrus, CA – cornu ammonis. Modified image obtained from Wikimedia Commons Public Domain search.
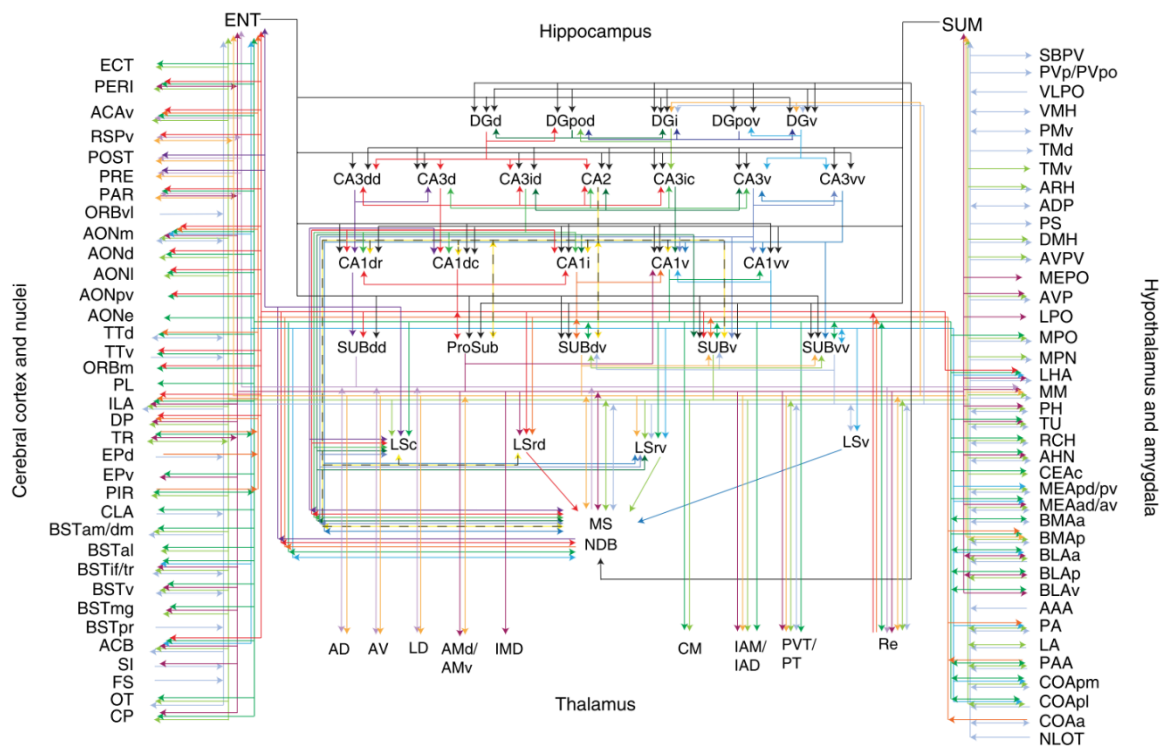
Figure 2 **Multiscale neural network of intra- and extra-hippocampal connections.** Connectome wiring diagram of all inputs and outputs of distinct hippocampal regions characterized by gene expression profiles (Bienkowski et al., 2018).

1.1.2. Early neural development of hippocampus

The development of the CA area, also known as *Cornu Ammonis,* starts in the prenatal period and extends up to four weeks after birth (CA area is subdivided into four main subfields: CA1-CA4). Neural progenitor cells of hippocampal pyramidal neurons are mainly derived from ventricular zone stem cells and they migrate radially until settling onto the hippocampal plate (Angevine, 1965). The CA1 and CA3 pyramidal neurons follow a similar developmental time course: the neurogenesis of their progenitor cells peaks between embryonic days E14-E16 (Hayashi et al., 2015). The laminar formation during the early stages of development is poles-inward driven, meaning that the neurons born earlier form the deeper part of the pyramidal cell layer, while those born later pass the older ones and align more superficially. The peak of synaptogenesis of CA1 neurons appears between two to four weeks postnatally (Steward and Falk, 1991), while for CA3 neurons it is reported to span from P3 to P21 (Lanore et al., 2012; Marchal and Mulle, 2004).

Unlike CA pyramidal cells, most of the granule cells of the dentate gyrus are generated only after birth (around 70%), during the first two weeks of postnatal development (Altman and Bayer, 1990). On the second – third postnatal week, Mossy fibers – the axons of granule cells – form connections with dendritic spines of CA3 pyramidal cells (Amaral and Dent, 1981).

1.1.3. Sex-dependent development of hippocampus

Even though there is a fair understanding on how hippocampal neurons develop during postnatal development, the foundation of this knowledge is based on single-sex research in males. Meanwhile, extensive studies have shown paramount quantitative and qualitative differences in male and female structure and function of the adult brain (Yagi and Galea, 2019). However, there is a lack of research that addresses the developmental pathways by which these sex differences are shaped.

Initially, only well-known sexually dimorphic regions of the brain, such as preoptic area, were investigated with anticipation to reveal sex-dependent variation in brain morphology and functional mechanisms at play. However, the first evidence that started a train of research of sex differences in hippocampus was the discovery that the morphology of CA1 pyramidal neurons varied in females according to the estrous cycle (Figure 3). In particular, proestrous female rats were shown to have greater apical dendritic spine density in CA1 pyramidal neurons compared to males and diestrous females (Elizabeth Gould et al., 1990). Interestingly, gonadal hormones were found to be the major regulators of spine density in this particular phenomenon.
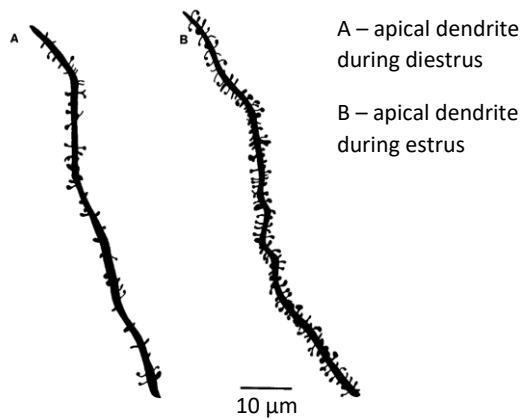
A – apical dendrite during diestrus

B – apical dendrite during estrus

10 µm

Figure 3 **Drawings of the apical dendrites of hippocampal CA1 pyramidal neurons in female rats** (Elizabeth Gould et al., 1990). Apical dendrite spine density during diestrus (**A**) is significantly lower than during estrus (**B**).

To some extent, sex differences in hippocampus can be attributed to the influence of steroid hormones. The hippocampus has high expression of sex hormone receptors, such as estrogen receptors (ERα, ERß) or androgen receptors (AR), that are distributed in a sex-specific and region-specific manner. For example, hippocampal areas CA3 and CA4 of adult female rats have a higher expression of ERß when compared to male rats (Zhang et al., 2002); depending on the phase of the estrous cycle, males have higher levels of AR in CA1 and dentate gyrus (Feng et al., 2010). There are also notable sex differences in the distribution of AR and ER in hippocampus during development (Mogi et al., 2015).

In addition to sex differences of hormonal receptor distribution, there are great differences in the morphology and electrophysiological properties of hippocampal neurons. Studies have revealed sex differences in the morphology of granule and pyramidal neurons of the rat hippocampus, such as more extensive branching of basal dendrites of CA3 pyramidal neurons in female rats (E. Gould et al., 1990) or greater dendritic intersections in granule neurons of the DG in males (Juraska et al., 1989). Interestingly, AMPA/NMDA receptor ratio is greater in females when compared to males (Monfort et al., 2015). In turn, there are sex differences in hippocampal LTP (Qi et al., 2016) and in neuron excitability (Warren et al., 1995).

There are multiple neurodevelopmental disorders that exhibit higher prevalence in a single sex, such as autism and schizophrenia (McGrath et al., 2004; Werling and Geschwind, 2013). These disorders could be potentially associated with the defects in sex-specific developmental mechanisms. An interesting field of research of glial contribution to the sex-dependent maturation of the brain can help to uncover some of these fundamental questions about sex-specific development. First and foremost, microglia is associated with the sexual dimorphism of brain differentiation and behavior in general (Lenz et al., 2013) and has been shown to exhibit sex-dependent morphological differences during pre- and postnatal stages of development (Nelson et al., 2017; Schwarz et al., 2012). It has been shown that

glial cells are critical for synaptic pruning during postnatal brain development (Paolicelli et al., 2011). Moreover, dysfunctional microglial cells are associated with neurodevelopmental disorders, including already mentioned autism and schizophrenia (Sekar et al., 2016; Werling et al., 2016). These studies suggest that microglia might be involved in sex-specific mechanisms that might be accountable for normal and/or disrupted development of the brain.

In 2017, Weinhard and Neniskyte et al., have looked into the sex-dependent synapse development in the early postnatal hippocampus. The morphology of microglia, together with the morphology of pre- and postsynaptic structures was investigated throughout the sensitive postnatal period of synaptic refinement. The results revealed that the volume and phagocytic capacity of microglia peaked and was resolved earlier in females than in males. These findings are in accordance with the differences in the density of neuronal spines and boutons. However, this study did not include any functional neuronal activity data.

In the light of the above, we must conclude that there are undeniable and potentially essential sex-dependent differences of synapse growth, reorganization, and maturation. It is of great importance to re-evaluate the electrophysiological activity profiles of postnatal development by including sex as a variable in order to uncover the sex-dependent mechanisms that shape the maturing brain.

1.2. The postnatal development of hippocampal CA1 pyramidal neurons

During four weeks of postnatal development, CA1 pyramidal cells undergo substantial changes in their intrinsic neuronal properties to acquire the characteristics of mature pyramidal neurons. One of the most apparent changes during postnatal maturation is the increase of the surface area of the neuronal membrane due to the expansion of the soma and the arborization of the dendritic tree (Schwartzkroin, 1981). Concurrently, input resistance and the values of the time constant are observed to decrease (I Spigelman et al., 1992). The slow membrane time constant depends on both the resistance and capacitance of the neuronal membrane. Because there are no apparent changes in the specific membrane capacitance, the decrease in the slow membrane time constant could be explained by the decreasing specific membrane resistivity, most probably due to the change in the density of ionotropic channels (Mccormick and Prince, 1987).

The maturation of the properties of neuronal membrane in turn shape the parameters of action potentials. During the postnatal period, action potentials of CA1 neurons are observed to increase in amplitude and to decrease in duration, while also becoming more rapid in both rising and falling phases (McCormick and Prince, 1987). These changes could not be attributed only to the resting potential of the membrane, suggesting there are postnatal changes in the density and the kinetics of ionic channels

that regulate the generation of action potentials. Additionally, frequency versus injected current relationships in general are less steep in immature neurons compared to the mature ones (McCormick and Prince, 1987).

1.3. The transformation of the synapses in the developing brain

The maturation of intrinsic properties of CA1 neurons coincide with the period of proliferation and refinement of synaptic connections. During postnatal development, both humans and other animals undergo a period of vigorous synaptogenesis that leads to an exponential increase of newly formed synaptic connections in the brain (Huttenlocher and Dabholkar, 1997). Followed by this increase, a selective reorganization of neural networks begins. Some synapses are maintained and strengthened, while functionally redundant ones are silenced or eliminated. This phenomenon is known as synaptic pruning and is thought to be crucial for normal development of synapses and for the maturation of characteristic neural pathways (Paolicelli et al., 2011). There have been abundant studies on the shaping of specific synaptic inputs such as neuromuscular junction or visual system (Neniskyte and Gross, 2017), although the data concerning other brain areas, such as hippocampus, are sparse. Brain imaging and *post-mortem* research suggest that abnormal synaptic pruning is potentially associated with neurodevelopmental disorders such as schizophrenia, autism and epilepsy (Neniskyte and Gross, 2017). For these reasons it is important to evaluate and to pinpoint the exact cellular mechanisms underlying the physiological reorganization of the synapses in health and disease.

1.3.1. The excitatory effect of GABA on maturing pyramidal neurons

The formation of functional synapses in the hippocampus is highly complex, with multiple mechanisms at play. One of the possible stimulants for the synaptic growth in hippocampus during postnatal development is the excitatory effect of GABA neurotransmission. At the end of the last century, scientists have found that in the developing nervous system GABA neurotransmitter elicits excitatory trophic activities, such as promoting synaptogenesis (Barbin et al., 1993). It has been observed that the formation of GABAergic synapses precedes and can modulate the emergence of glutamatergic synapses. The explanation for this phenomena has been first described by (Ben‑Ari et al., 1989). The initial excitatory role of GABA is thought to be the result of a high intracellular concentration of chloride. Additionally, giant depolarizing potentials observed in all developing circuits are in part generated by the excitatory effects of GABA. These giant depolarizing potentials allow large oscillations of intracellular calcium, which in turn can trigger activity-dependent modulation of neuronal growth

and synapse formation. After the sufficient density of GABAergic and glutamatergic synapses is achieved, activity-dependent chloride-extruding system is initiated. Once the chloride inside the neuron can be operatively flushed out, GABA exerts its conventional inhibitory action.

In neonatal hippocampus, the activation of GABA type A receptors in CA3 pyramidal neurons leads to a membrane depolarization that is sufficient to remove the voltage-dependent magnesium block of NMDA receptors (Leinekugel et al., 1997). Therefore, GABA can activate NMDA receptors and increase the intracellular concentration of calcium in neonatal neurons. It is also known that granule cells express a GABAergic phenotype as they have the immunoreactivity to GABA decarboxylase. The excitatory effect of GABA on CA3 neurons transitions to an inhibitory as the neurons mature. This shows that the GABAergic transmission of the mossy fibers might potentially accompany the morphological maturation of pyramidal cells, possibly until the development of dendrites and spines is completed (Amaral and Dent, 1981). It is now believed that developmental transition of GABA activity from the excitatory to the inhibitory is essential for maintaining the equilibrium between excitation and inhibition in order to prevent dire pathological consequences that arise either from hyperexcitability or excessive inhibition of maturing networks (Ben-Ari, 2002).

1.3.2. Silent synapses and AMPA/NMDA ratio

Another piece of the synapse development puzzle is the silent synapses. The notion of silent synapses stems from the observations of a mismatch between the number of morphologically identified synapses and the number of functional ones (Atwood and Wojtowicz, 1999). For example, it is thought that more than 95% of ~100 000 synapses between the Purkinje and granule cells might be silent. Given these numbers, the process of synaptic silencing or unsilencing seems to be a prominent feature of the adult brain. However, silent synapses have first been detected and are the most extensively studied in the developing brain.

A typical glutamatergic synapse contains two main types of ionotropic glutamate receptors, particularly NMDARs and AMPARs (Figure 4). AMPARs are ligand-gated, rapid transmission ion channels, able to induce quick local depolarization of the membrane. In comparison, NMDARs are also voltage-gated and contain a Mg^{2+} block that is released only at highly hyperpolarized potentials, when the receptors become conductive to cations. AMPA-silent synapses contain only functionally active NMDARs, thus are silent at the resting membrane potential, yet can conduct NMDAR mediated currents at depolarized membrane potentials. It is still debated whether silent synapses lack AMPARs (Kerchner and Nicoll, 2008), or the existing AMPARs are not able to facilitate transmission (Choi et al., 2000; Groc et al., 2002).
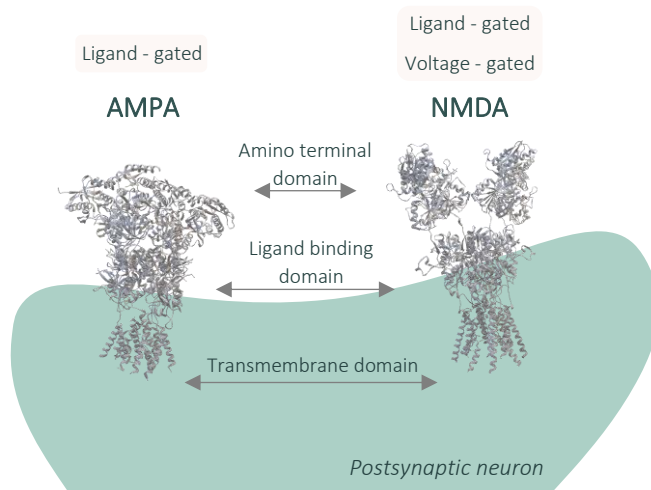
Figure 4 **A prototypical glutamatergic synapse** containing two main types of ionotropic glutamate receptors: NMDAR and AMPAR. 3D structures of the receptors were obtained from RCSB Protein Databank.

The transition process from a silent synapse to a mature glutamatergic synapse is thought to be a multistep process involving both the changes of AMPAR and NMDAR subunits as well as the rearrangement of postsynaptic density (PSD) proteins (Tsai et al., 2012). Experimentally, AMPA unsilencing is typically initiated by a low-frequency presynaptic pairing with prolonged postsynaptic depolarization (Isaac et al., 1995). It is thought that during development $GABA_A$-mediated transmission might contribute to the unsilencing by depolarizing and promoting synchronous network activity in developing neurons (Ben-Ari, 2002). This synchronous network activity is associated with the development of the entire nervous system (Blankenship and Feller, 2010; Garaschuk et al., 1998) and is proposed to determine synaptic selection during synapse refinement (Katz and Shatz, 1996).

During the first few postnatal days, nearly all the hippocampal synapses between the Schaffer collateral and CA1 neurons are silent. By the second to third week approximately half of the synapses become unsilenced (Durand et al., 1996; Albert Y Hsia et al., 1998; Liao et al., 1995). These results are also supported by morphological studies (Pickard et al., 2000) and suggest that NMDARs are expressed first, followed by a delayed recruitment of AMPARs.

Neurodevelopmental disorders, including intellectual disability and autism spectrum disorders, are commonly associated with redundant circuit connectivity and immature spine morphology (Penzes et al., 2011). Animal models of these disorders also show aberrant numbers of silent synapses, suggesting that the distorted connectivity might stem from either premature and excessive or, on contrary, delayed synaptic pruning.

1.3.4. Spontaneous and miniature excitatory postsynaptic currents

During synaptogenesis, a rapid increase in the amplitude of spontaneous excitatory postsynaptic currents (sEPSCs) is observed, and can be attributed to an increase in the number of synapses per axonal input, arising from the regional emergence of synaptic connections (He et al., 2009; Albert Y Hsia et al., 1998). The amplitude of miniature excitatory postsynaptic currents (mEPSCs), on the other hand, mirrors the release of synaptic vesicles that is independent on the action potentials. Experimentally, mEPSCs are registered after application of sodium channel blocker TTX. Mean value of mEPSCs is often used as an estimate of quantal size (q), that is, a postsynaptic response size (amplitude) of a current to a single released neurotransmitter vesicle. Published data suggest that the amplitudes of mEPSCs remain constant over the period of postsynaptic development, arguing for a stable q. Although the mean q does not change, it has been shown that the variance of q decreased significantly during development, suggesting there is a tuning mechanism that allows to achieve the uniformity of quantal responses in mature brain (Albert Y Hsia et al., 1998).

1.3.5. Synaptic multiplicity

Synaptic multiplicity defines the number of functional synapses between a pair of two given neurons. Evaluating synaptic multiplicity can help to characterize the efficacy of synaptic transmission throughout postnatal development, under various physiological conditions, or in case of disease (Paolicelli et al., 2011; Salter et al., 2018; Zhan et al., 2014).

Synaptic multiplicity increases the efficacy of synaptic transmission. If neurons are connected by multiple synapses, an action potential will initiate a synchronous release of presynaptic vesicles from multiple axonal boutons. This will most likely result in the temporal summation of postsynaptic currents, leading to an increased apparent amplitude of recorded EPSC (Figure 5, A). If we were to apply TTX to the surrounding environment of such pair of neurons, observed postsynaptic currents would be action potential-independent. This way, the spontaneous release of synaptic vesicles would be asynchronous, resulting in reduced apparent amplitude of recorded EPSCs (Figure 5, B). Conversely, if a pair of neurons is only connected by a single synapse, the amplitude of recorded EPSCs without TTX and with TTX will remain constant (Figure 5, C). Multiplicity between rat hippocampal CA3-CA1 pyramidal neurons has been observed to increase two-fold from neonatal to adult ages (Albert Y. Hsia et al., 1998). The enhanced coupling between existing neuronal pairs might be one of the developmental strategies for strengthening the associations between CA3-CA1 neurons.
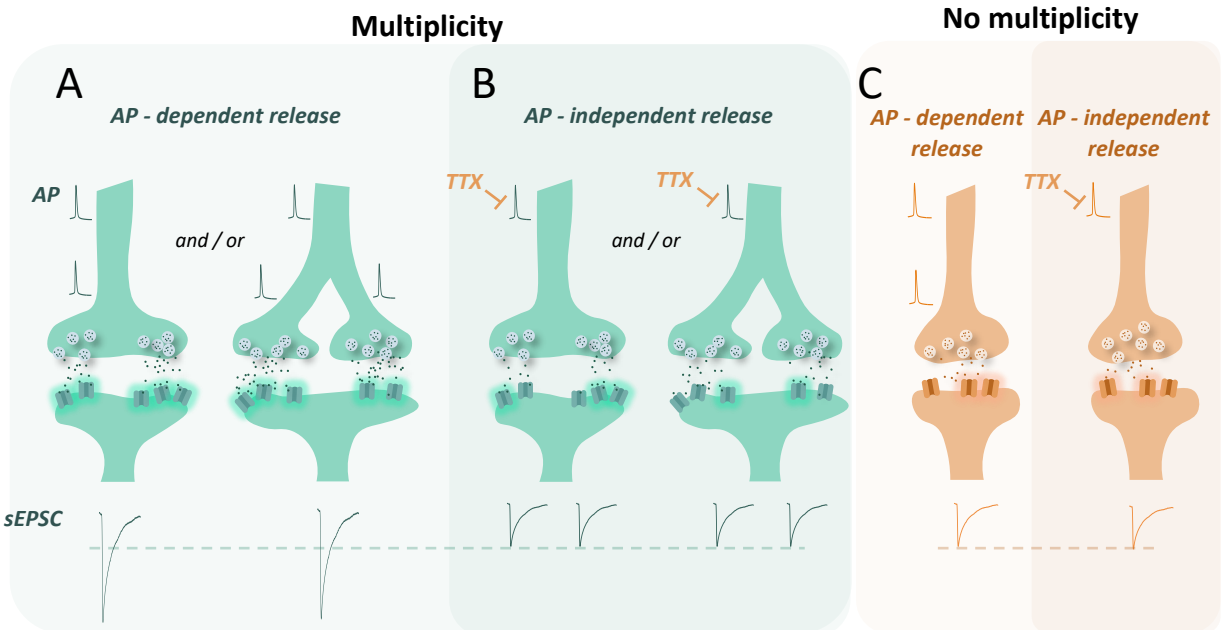
Figure 5 **Synaptic multiplicity reflected through recorded synaptic activity.** *A* If a pair of neurons has multiple synapses between them, an incoming action potential will result in a synchronous release of presynaptic vesicles, which will lead to temporal summation of EPSCs. *B* Application of TTX will block action potentials and the resulting release of vesicles will be asynchronous; hence recorded EPSCs will be quantal in size. *C* Recorded EPSCs from a pair of neurons with no multiplicity will be consistent in size without and with application of TTX. Illustration created by the author.

MATERIALS AND METHODS

2.1. Materials

All the materials, equipment and software that were used are specified below.

2.1.1. Chemicals and reagents

Name of reagent	Full name	Cat. No.
NaCl	*Sodium chloride*	**Sigma**: 746398
MgATP	*Adenosine 5'-triphosphate magnesium salt*	**Sigma**: A9187
Na_2GTP	*Guanosine 5'-triphosphate sodium salt hydrate*	**Sigma**: G8877
NaH_2PO_4	*Sodium dihydrogen phosphate*	**Sigma**: S5011
$NaHCO_3$	*Sodium bicarbonate*	**Sigma**: S5761
CsCl	*Cesium chloride*	**Sigma**: C4036
$CsMetSO_3$	*Cesium methanesulfonate*	**Sigma**: C1426
CsOH	*Cesium hydroxde*	**Sigma**: 232041
K-gluconate	*D-Gluconic acid potassium salt*	**Sigma**: P1847
EGTA	*Glycol ether diamine tetraacetic acid*	**Sigma**: E4378
Bicuculline	*Bicuculline*	**Sigma**: 14340
Qx314 bromide	*Lidocaine N-ethyl bromide*	**Sigma**: L5783
BAPTA	*1,2-Bis(2-Aminophenoxy)ethane-N,N,N',N'-tetraacetic acid*	**Sigma**: A4926
NMDG	*N-methyl-D-glucamine*	**Sigma**: 66930
Thiourea	*Sulfourea, thiocarbamide*	**Sigma**: T7875
Na-ascorbate	*(+)-Sodium L-ascorbate*	**Sigma**: 11140
Na-pyruvate	*Sodium pyruvate*	**Sigma**: P2256
Phenol red indicator	*Phenol red solution*	**Sigma**: P0290
$CaCl_2$	*Calcium chloride*	**Sigma**:C1016
Glucose	*α-D-glucose*	**Sigma**:G8270
HEPES	*4-(2-hydroxyethyl)-1-piperazineethanesulfonic acid*	**Sigma**:H3375
KCl	*Potassium chloride*	**Sigma**:P9333
$MgCl_2$	*Magnesium chloride*	**Sigma**: M8266
O_2 / CO_2 (95 % / 5 %)	*Dioxygen/Carbon dioxide (95 % / 5 %)*	**Elme Messer Lit**

2.1.2. Media, buffers and solutions

a) NMDG-HEPES aCSF Table 1

b) HEPES holding aCSF Table 2

c) HEPES recording aCSF Table 3

d) Na$^+$ spike-in solution (2M) Table 4

e) Intracellular solution Table 5

Ideally, aCSF solutions were made fresh on the day of the experiment. Otherwise, they were stored for use at 4 °C for up to 1 week. All aCSF solutions were saturated with carbogen (95% O_2 / 5% CO_2) prior to use to ensure stable pH buffering and adequate oxygenation. The pH of all solutions was adjusted to 7.3-7.4 and osmolarity measured and adjusted to 300-310 mOsmol/kg.

Table 1 **NMDG-HEPES aCSF**

Reagent	Final conc., *mM*	MM, *g/moL*	Amount for 1 L
NMDG	92	195.21	17.9593 g
KCl	2.5	74.55	0.186 g
NaH_2PO_4	1.25	119.98	0.15 g
$NaHCO_3$	30	84.01	2.5203 g
HEPES	20	238.3	4.766 g
Glucose	25	180.16	4.504 g
Thiourea	2	76.12	0.152 g
Na-ascorbate	5	198.11	0.9906 g
Na-pyruvate	3	110.04	0.3301 g
$CaCl_2*2H_2O$ (1 M $CaCl_2$)	0.5		0.5 mL
$MgSO_4*7H_2O$ (1 M $MgCl_2$)	10		10 mL
Titrate pH to **7.3 – 7.4** with **17 mL +/- 0.5 mL of 5M hydrochloric acid**. *NOTE*: This titration step should ideally be performed prior to the addition of divalent cations to avoid precipitation; however, the precipitation can be reversed upon adjustment of the pH to the physiological range.			

Table 2 **HEPES holding aCSF**

Reagent	Final conc., *mM*	MM, *g/moL*	Amount for 1 L
NaCl	92	58.44	5.3765 g
KCl	2.5	74.55	0.186 g
NaH_2PO_4	1.25	119.98	0.15 g
$NaHCO_3$	30	84.01	2.5203 g
HEPES	20	238.3	4.766 g
Glucose	25	180.16	4.504 g
Thiourea	2	76.12	0.152 g
Na-ascorbate	5	198.11	0.9906 g
Na-pyruvate	3	110.04	0.3301 g
$CaCl_2*2H_2O$ (1 M $CaCl_2$)	2		2 mL
$MgSO_4*7H_2O$ (1 M $MgCl_2$)	2		2 mL
Titrate pH to **7.3–7.4** with several drops of concentrated 10N NaOH			

Table 3 **HEPES recording aCSF**

Reagent	Final conc., *mM*	MM, *g/moL*	Amount for 1 L
NaCl	124	58.44	7.247 g
KCl	2.5	74.55	0.186 g
NaH_2PO_4	1.25	119.98	0.15 g
$NaHCO_3$	24	84.01	2.016 g
HEPES	5	238.3	1.192 g
Glucose	12.5	180.16	2.252 g
$CaCl_2*2H_2O$ (1 M $CaCl_2$)	2		2 mL
$MgSO_4*7H_2O$ (1 M $MgCl_2$)	1		1 mL
Titrate pH to **7.3–7.4** with several drops of concentrated 10N NaOH			

Table 4 **Na^+ spike-in solution (2M)**

For each brain slice preparation 580 mg of NaCl was dissolved in 5 mL of freshly prepared NMDG-HEPES aCSF.

Table 5 **Intracellular solution**

Reagent	Final conc., *mM*	MM, *g/moL*	Amount for 20 mL
K-gluconate	140	234.246	0.6559 g
KCl	5	74.55	0.0075 g
EGTA	5	380.35	0.038 g
HEPES	10	238.30	0.0477 g
$CaCl_2$ (100 mM)	0.5		100 µL
$MgCl_2$ (100 mM)	0.5		100 µL
Mg-ATP/Na_2-GTP	2/0.3		Added on the day of the experiment
Fill to 19.2 mL with ddH_2O; pH **7.4** and 315 mOsmol/kg			

2.1.3. Equipment

Device	Producer
Dissection tools	Ted Pella
pH meter	Hanna Instruments
Osmometer *Osmomat 3000*	Gonotec
Vibratome *Vibrating microtome 5100 mz*	Campden Instruments Ltd
Peristaltic pump *Peri-Star™ Pro*	World Precision Instruments
Microcapillary puller *Puller P1000*	Sutter Instruments
Microscope *Fixed Stage Microscope ECLIPSE FN1*	Nikon Corporation
Multi – manipulator Controller *MPC-200* and Input device *ROE-200*	Sutter Instrument
Analog-to-digital converter *Digidata 1440A*	Molecular Devices
Amplifier *MultiClamp 700B*	Axon Instruments
Perfusion chamber	Custom made
Brain slice recovery chamber	Custom made
Brain slice anchor	Custom made

2.1.4. Software

Software	Source
Clampex	Axon Instruments, Union City, CA
Clampfit	Axon Instruments, Union City, CA
OriginPro 9.0	OriginLab Corporation
AutoCAD	Autodesk Inc.

2.2. Methods

2.2.1. Animals

All animals were group housed and kept on a 12 hours light/dark cycle (lights on 7:00 - 19:00) with a constant temperature (21.5 ± 1 °C) and humidity (55 ± 8 %). Water and food were given *ad libitum*. Animals were used in accordance with the guidelines on the ethical use of animals from the European Communities Council Directive of November 24, 1986 (86/609/EEC). Efforts were made to minimize animal suffering and to reduce the number of laboratory animals used, in accordance with the European Communities Council Directive of September 20, 2010 (2010/63/UE).

2.2.2. Acute brain slice preparation

Acute brain slice preparation was adapted from a NMDG protective recovery method, described by Jonathan T. Ting (Ting et al., 2018). This method optimized aCSF media for brain slicing and recovery to acquire healthy brain slices suitable for patch clamp electrophysiology. The main component differing from other aCSF media formulations was N -methyl-d-glucamine (NMDG), which was used instead of the main salt (NaCl) in aCSF media that is used during brain dissection and vibratome slicing to reduce the overall excitability of the acute slices increasing neuronal preservation. Among various other sodium ion substitutes such as sucrose, choline, glycerol and Tris, NMDG has been shown to be the most versatile and effective (Ting et al., 2018). Additionally, the aCSF was supplemented with HEPES to sustain pH buffering and to prevent brain slice edema; additional supplements such as ascorbic acid thiourea lower the effects of oxidative stress. An additional step of brain slice recovery (Na^+ spike-in) was added to slowly reintroduce sodium to the aCSF. One of the main advantages of this method considering this particular study was the adaptability to a wide range of animal ages ensuring same preparatory conditions and neuronal health throughout various postnatal development stages.

Acute brain slice preparation in this study was structured into three main parts: brain dissection, vibratome slicing and brain slice recovery (see the graphical summary in Figure 6):
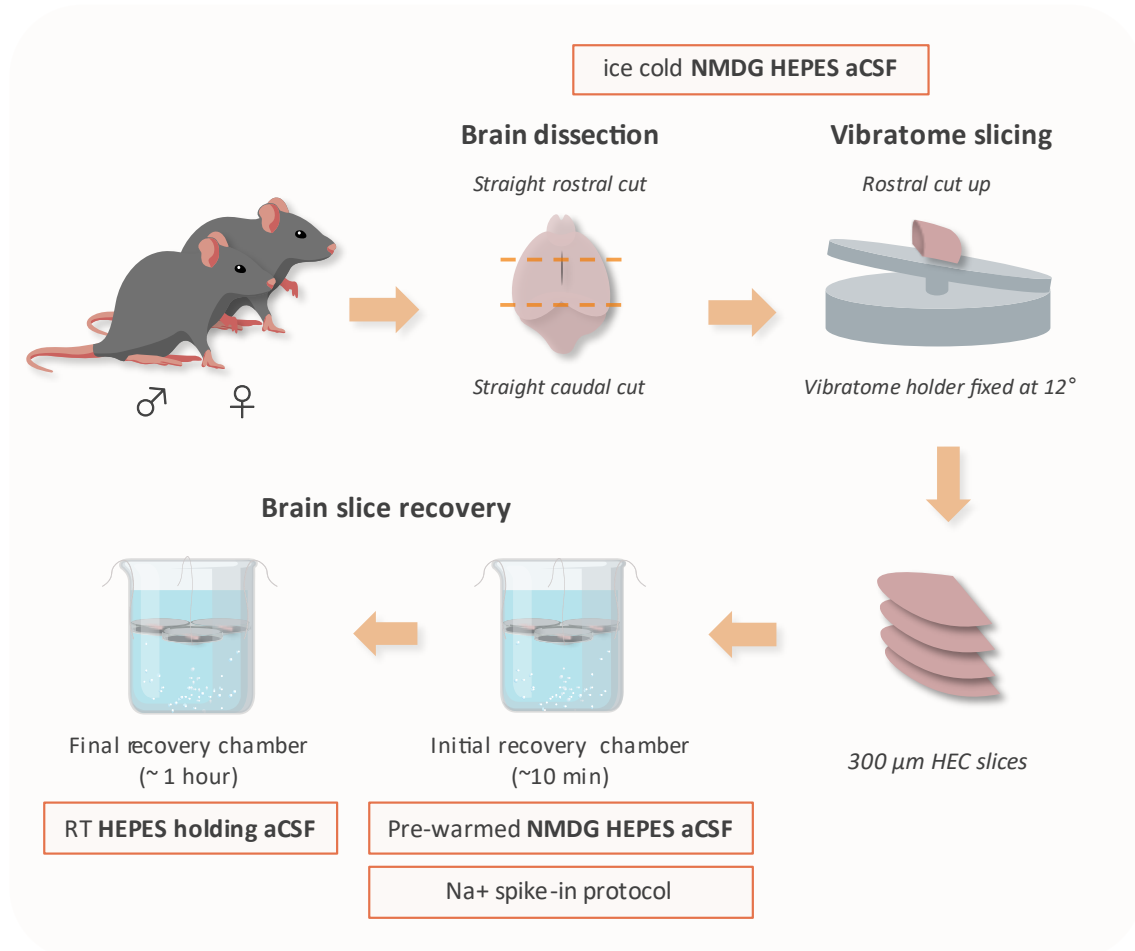

Figure 6 **Graphical abstract of acute brain slice preparation.** Brain slice preparation involves three main steps: brain dissection, vibratome slicing and brain slice recovery. Boxes in orange indicate solutions used for the particular brain slice preparation step. *HEC* - Horizontal Entorhinal Cortex.

Brain dissection

For mouse brain dissection the slicing station and dissection instruments were prepared as illustrated in Figure 7 and Figure 8. Wild type male and female mice of various postnatal ages were culled by cervical dislocation and then were decapitated with large laboratory scissors. The head was then briefly dipped in chilled and carbogenated (95% O_2 / 5% CO_2) NMDG HEPES aCSF. The skin was cut off with precision scissors to expose the skull. The head was then stabilized by securing it with tweezers through the eye sockets. A careful cut was made along the midline caudorostrally with delicate scissors. The head was again briefly dipped in chilled and carbogenated NMDG HEPES aCSF. Using fine forceps, the skull bones were pulled to the sides without pressing or damaging the brain. The brain was taken out

of the skull with a flat spatula and submerged into chilled and carbogenated NMDG HEPES aCSF for one minute. The brain was then placed on a Whatmann filter paper in a Petri dish hallway filled with chilled and carbogenated NMDG HEPES aCSF. To prepare HEC slices the rostral and caudal parts of the brain were cut with a scalpel at a right angle (See Figure 9). Optionally the brain was additionally cut in half caudoventrally to separate the hemispheres. The brain was swiftly dried up with a piece of filter paper and glued onto the angled (12°) vibratome holder with the ventral side positioned down and rostral part facing up the angle.
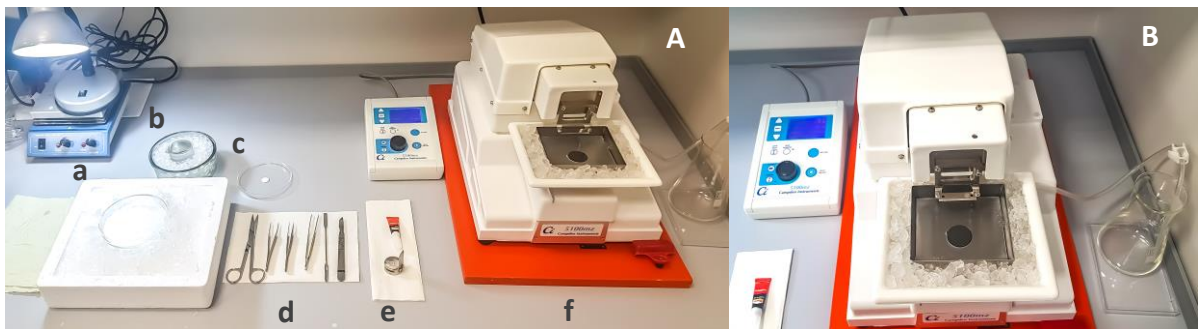

Figure 7 **The setup of a slicing station *A a*** a wide plastic Petri dish is prepared for the dissection of the brain ***b*** a small glass beaker nested in ice is prepared to submerge the brain after the removal from the head; additional larger beaker is prepared (also nested in ice, not shown in the picture) for the submersion of the head during the brain extraction procedure ***c*** A Petri dish with a Whatmann filter paper is prepared to be used for the dissection of the brain ***d*** surgical instruments are placed in order ***e*** super glue will be used to glue the brain to the vibratome holder ***f*** prepared vibratome ***B*** prepared vibratome should be filled with carbogenated NMDG-HEPES aCSF, filled with ice from the sides; the melting ice is collected to a separate beaker***.***

Figure 8 **The placement of the surgical instruments** (from left to right): large laboratory scissors (for decapitation); delicate scissors (for cutting off the skin and cutting the skull); sturdy tweezers (for holding the head through the eye sockets); blunt rough tip tweezers (for opening the skull); spatula (for taking out the brain); scalpel (for cutting the brain); also placed on the side are super glue and vibratome holder;
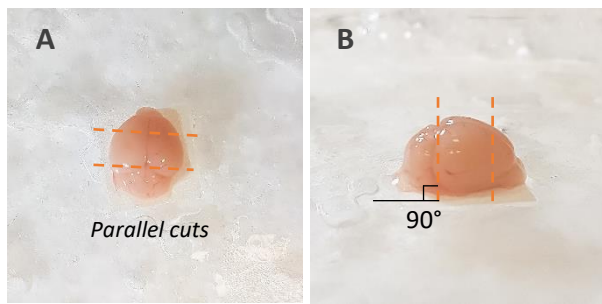
Figure 9 **Brain cutting scheme**; orange lines indicate the cutting lines and angles *A* view from the top for the location of the rostral and caudal cuts *B* a view from the side: cutting angles for the rostral and caudal parts.

Vibratome slicing

Prior to cutting the slices with a vibratome, the slicing parameters were set to: slicing thickness – 300 μm; horizontal movement frequency – 80 Hz; movement amplitude – 1.5 mm; slicing speed – 0.1 mm/s (the speed was 0.25 mm/s when removing the top layers of the brain without the hippocampus). The slicing procedure was performed with a steel blade. The slicing vibratome bath was filled with chilled and carbogenated NMDG HEPES aCSF; the sides of the slicing bath were loaded with ice. The vibratome holder with the secured brain was positioned in a way that the blade reached the dorsal part of the brain first.

Brain slice recovery

After cutting the slices they were transferred with a wide plastic pipette to a custom-made initial brain slice recovery chamber (see RESULTS for how the chamber was made) filled with a pre-warmed (32°C - 34°C) and continuously carbogenated NMDG HEPES aCSF. Within the 10 minutes of transferring the acute brain slices, sodium ions were gradually introduced into the NMDG HEPES aCSF as indicated in Table 6:

Table 6 **Na$^+$ spike-in protocol.** Volumes adjusted for 150 mL aCSF and 2M NaCl. Adjust volumes or concentration of NaCl accordingly.

Time, min	Volume, μL	Final conc. of Na$^+$ in buffer, mM
0	250	3.3
2	250	6.6
4	500	13.2
6	1000	26.5
8	2000	52
10	Transfer to **HEPES holding aCSF**	92

After Na⁺ spike-in protocol was complete, the slices were transferred to a final custom-made recovery chamber filled with continuously carbogenated HEPES holding aCSF at room temperature. The slices were resting in this recovery chamber for at least one hour prior to recording.

2.2.3. Whole-cell patch clamp recording

To record electrophysiological data, acute brain slices were transferred to a perfusion chamber and secured with a brain slice anchor (both custom-made, see RESULTS for more details). The perfusion chamber was secured to the electrophysiology recording station table to ensure stability throughout the experiment. The brain slice was continuously perfused with carbogenated HEPES recording aCSF (2 mL/min – 5 mL/min) at room temperature. Hippocampal CA1 pyramidal neurons were patched in whole-cell configuration with patch clamp technique (Figure 10). Borosilicate glass micropipettes were pulled to 3 MΩ - 8 MΩ and then filled with freshly thawed and filtered intracellular solution. When recording synaptic activity, Qx314 was added to block sodium action potentials and postsynaptic GABA$_B$ receptors. Recording location was identified via 4X magnification objective with brightfield microscopy. Subsequently, the objective was switched to a 40X magnification to identify individual neuron bodies in a pyramidal cell layer of hippocampus CA1b area. To ensure a clean pipette tip, a subtle positive pressure was applied through a 1 mL syringe and secured with a three-way valve while lowering the pipette to the slice. A small dimple formed in the membrane when the pipette reached the surface of the cell. Positive pressure was quickly swapped to a gentle suction until Gigaohm seal formed. To break into the cell and acquire whole-cell configuration, swift pulses of negative pressure were applied either by suction or a syringe. Ideally, recordings were performed on cells that were located >30 μm deep in the slice, as there was less chance for the neurons to be physically damaged with severed dendritic processes. Only medium-sized cells with a homogenous surface appearance and soft membrane boundaries were chosen to be patched. Data were sampled at 20 kHz with a 16-bit analog-to-digital converter *Digidata 1440A* and displayed using *pCLAMP* software. Resting membrane potential and input resistance for every neuron were calculated from the incremental step waveform function in a voltage-clamp configuration. Neurons with a resting membrane potential below a standard firing threshold (negative to -55 mV) were accepted for further analysis. Experiments were performed within 8 hours after slicing. Animal age or sex was known during recordings.
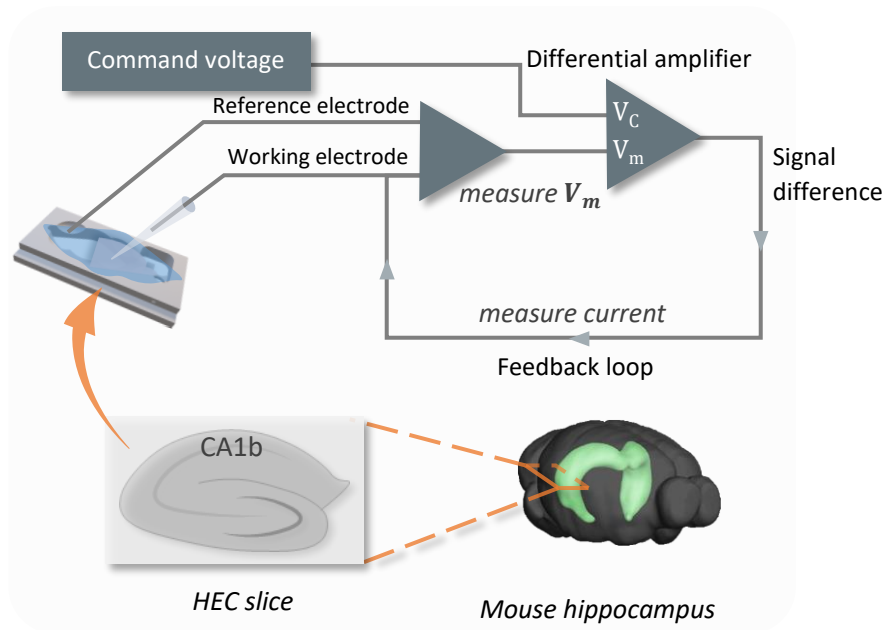
Figure 10 **Simplified illustration of patch clamp circuitry.** Mouse brain obtained from Allen mouse brain atlas.

2.2.4. Recording and analyzing sEPSCs and mEPSCs

Spontaneous excitatory postsynaptic currents were recorded by clamping a neuron at rest (-70 mV) for 10 minutes in a voltage-clamp configuration. Miniature EPSCs were recorded in the same way, additionally applying 0.5 µM TTX to the perfusion system to block action potential-dependent events. The recording of mEPSCs started 6-10 minutes after the application of TTX to ensure the full effect of the drug. Recorded signals were low pass filtered with a 500 Hz Gaussian filter and analyzed using *Clampfit* and *OriginPro* software. sEPSCs and mEPSCs were identified on the basis of a template that was created in *Clampfit* (Create Template function) using 20-30 single events. All events were recognized through the template search function in *Clampfit*, with a template match factor of 2.5. To evaluate consistency of the synaptic responses, all recordings underwent a "sanity check" by graphing the amplitudes of the accepted events in time. A normal physiological activity resulted in a homogenous distribution of the amplitudes in time. In case of abnormal or burst-like activity, either the irregular data interval was cut out or the whole recording was rejected for further analysis. Mean peak amplitudes and mean interevent intervals were calculated for each individual neuron by averaging the values of all events. To calculate these values for each developmental stage, all of the events were pooled and averaged from neurons belonging to the same developmental interval. Cumulative probability graphs were generated by calculating cumulative frequencies and subsequently normalizing them.

2.2.5. Calculating synaptic multiplicity

Synaptic multiplicity was calculated by a formula first described elsewhere (Albert Y. Hsia et al., 1998):

$$Multiplicity = \frac{a}{q},$$

where *a* stands for the mean amplitude of action potential dependent EPSCs, and *q* is a mean quantal size that is defined as a mean amplitude of miniature EPSCs obtained in the presence of TTX (action potential independent events). To calculate *a,* the contribution of mEPSCs is subtracted from the pool of all of the events recorded without TTX. To achieve that, the authors proposed *b* to stand for a mean amplitude of both sEPSCs and mEPSCs recorded in absence of TTX, and v_{events} equal to the frequency of sEPSCs (v_a) or mEPSCs (v_q). This way it is possible to express *b* as a frequency weighted average of *a* and *q:*

$$b = \frac{v_a \cdot a - v_q \cdot q}{v_b}$$

And now to rearrange the equation for *a:*

$$a = \frac{v_b \cdot b - v_q \cdot q}{v_b - v_q}$$

v_b and *b* are obtained from a signal recorded in absence of TTX, and v_q and *q* are calculated from a signal recorded in presence of it. *a* to *q* ratio is the final multiplicity value.

2.2.6. Recording and analyzing action potentials

Action potentials were recorded in current-clamp mode. A current was injected into the cell by a step waveform function that increased in magnitude with every sweep. A magnitude of injected current was selected for neurons individually by finding a rheobase (a current that triggers an action potential response). A representative waveform signal is shown in Figure 11. A train of action potentials was observed as a response to the injected current. The recorded sweeps were analyzed in *Clampfit* and *OriginPro* software. Action potential features used in further calculations are illustrated in Figure 12.

Figure 11 **A representative rectangle current stimulus** contains multiple step increments that increase in height with every sweep. Length of a step is one second. The magnitude of the injected current varied from neuron to neuron.
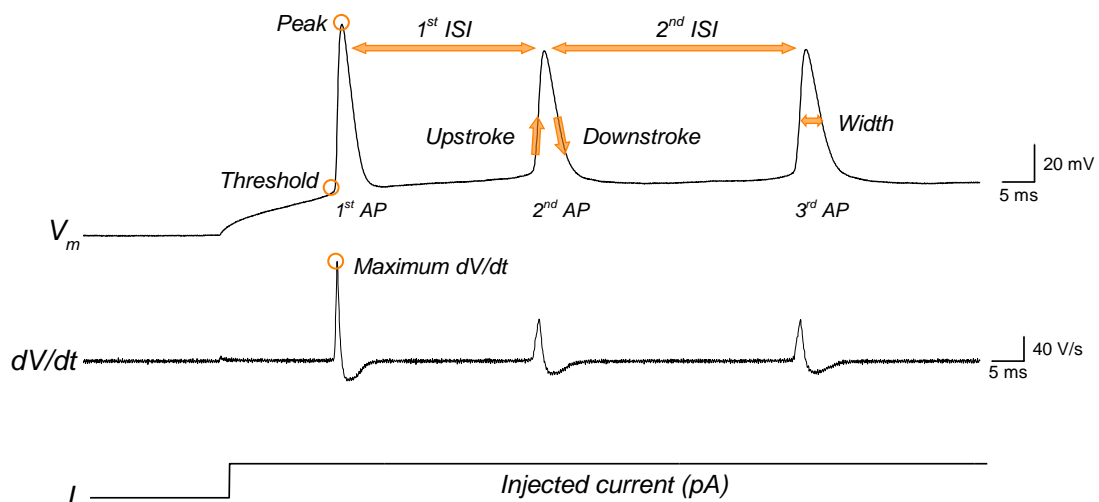
Figure 12 **Illustration of action potential features.** First three action potentials (top) evoked by a long square stimulus (bottom) with various features identified. Derivative values (middle) were directly calculated from a voltage trace. ISI - Interspike interval; AP – Action potential; See text for definitions.

Action potential peak

Action potential peak was defined as a maximum value of the membrane potential during the action potential. All of the action potential peak values for all sweeps were detected with a Peak Analyzer function in *OriginPro* software (Figure 13, A, B). To obtain mean action potential peak values for individual neurons, all peak values of first action potentials in every sweep were averaged. Distances

between two consecutive peaks were called interspike intervals (ISIs). Action potential firing rates (spikes per second) were calculated for every interspike interval in every sweep (Figure 13, C).
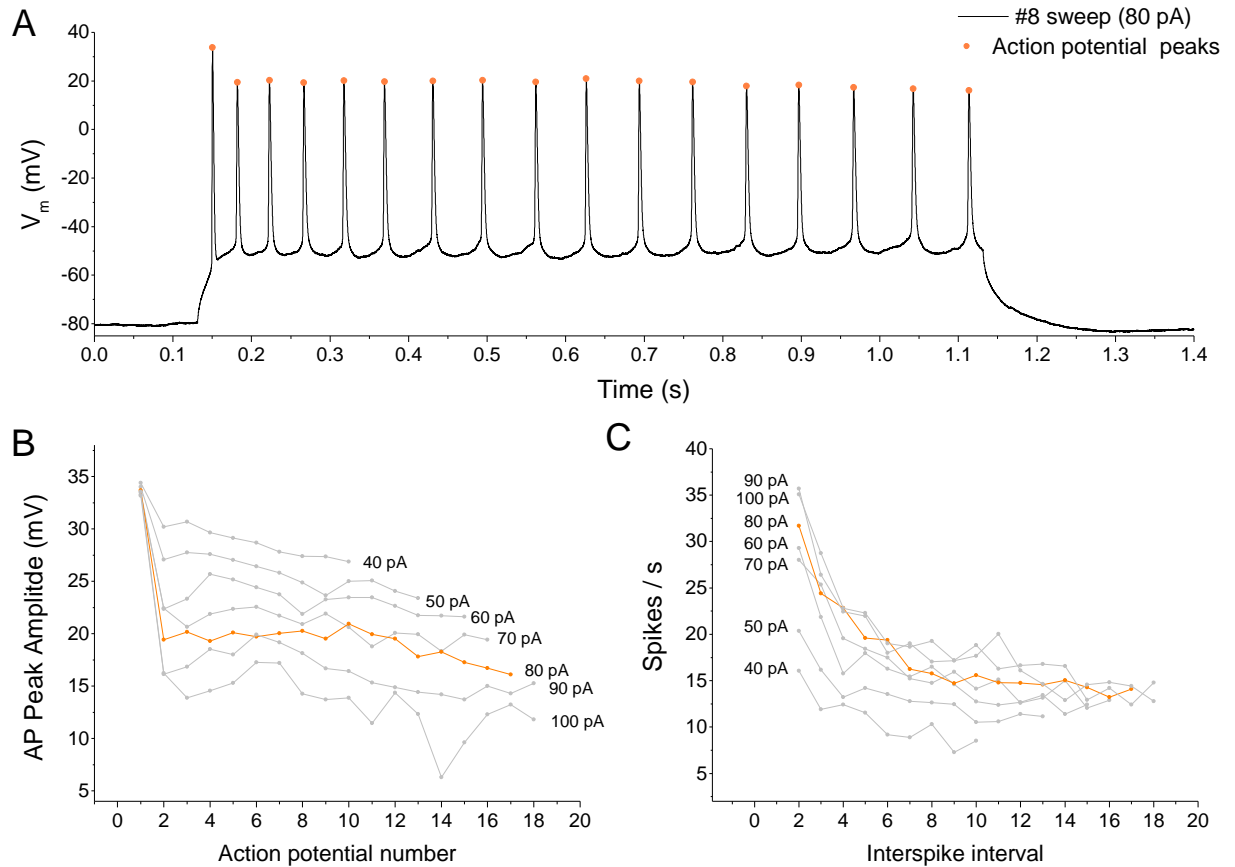
Figure 13 **Investigating action potentials. *A*** A representative sweep of action potential train recorded in current-clamp mode. To investigate action potential properties, a second-long square waveform current was injected into the cell. The injected current value was increased incrementally with each sweep. Orange dots represent action potential peaks detected with Peak Analyzer function in *OriginLab* software. ***B*** Action potential peak amplitudes obtained for every action potential in every sweep. Orange line indicates peak values for a representative sweep. ***C*** Firing rate values for every interspike interval in every sweep.

Firing frequency adaptation index

To investigate the rate at which action potential firing speeds up or slows down during a stimulus, adaptation index was calculated as:

$$\frac{1}{N-1}\sum_{n=1}^{N-1}\frac{ISI_{n+1}-ISI_n}{ISI_{n+1}+ISI_n}$$

Where *N* is the number of ISIs in a trace. All of the traces above and including the trace with a highest average firing rate (most action potentials in a single trace) are averaged and plugged into the formula to obtain a single value for each recorded neuron. This equation is used for electrophysiological characterization of neurons in Allen Cell Types Database project at the Allen Institute for Brain Science.

Action potential threshold

An action potential threshold value (Figure 14, A) was arbitrarily defined as a voltage value at the first time point when the derivate *dV/dt* during the upstroke of the action potential was higher than 10 V/s (Figure 14, B – orange interval). The derivative traces of action potentials were found in OriginPro software, then filtered to select the appropriate time points. These time points represented action potential thresholds in a voltage trace. Figure 14, C shows a full set of calculated threshold values for each action potential in every sweep for a single neuron. Because the depolarizing current influences the threshold values of action potentials in time, a mean threshold value for an individual neuron was calculated as an average value of all first threshold values in every sweep.
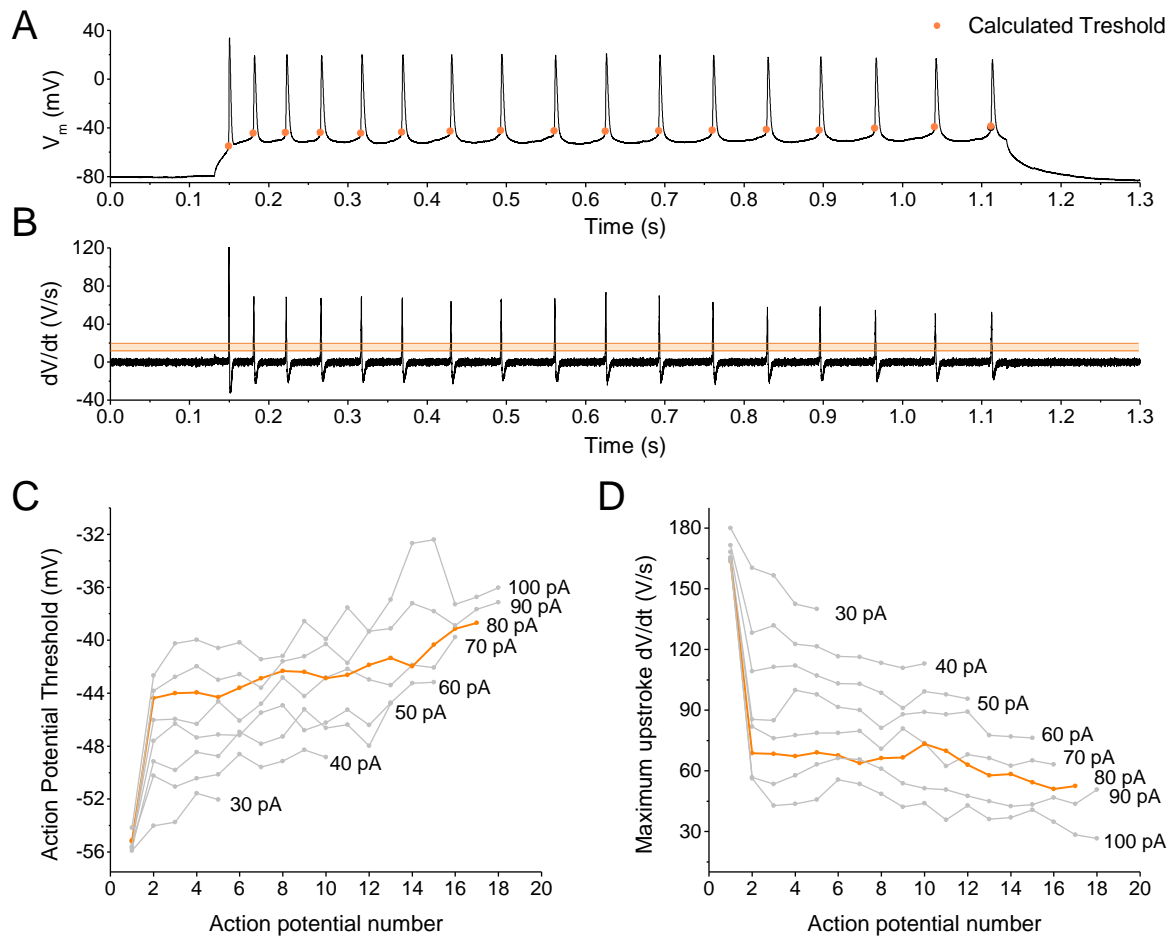
Figure 14 **Obtaining derivatives and threshold values. *A*** Representative voltage sweep with calculated threshold values for each action potential. ***B*** Derivative function of a representative trace reveals the speed at which action potentials depolarize and repolarize. It is tightly related to ion channel density and function and can be one of the indicators of neuronal maturity. Threshold values are extracted by arbitrarily selecting the time points where the derivative values are more than 10 V/s and most of the time less than 20 V/s (marked in orange). ***C*** Calculated threshold values for action potentials in all sweeps. Orange line indicates action potential thresholds of a representative sweep. ***D*** Calculated maximum upstroke dV/dt values for each action potential in every sweep.

Maximum upstroke and downstroke dV/dt of AP

Maximum upstroke and downstroke dV/dt values were defined as the highest upstroke or lowest downstroke values of the action potential derivative trace. Maximum dV/dt values were found with a Peak Analyzer function in *Origin* software. Mean maximum derivative values for a single neuron were calculated by averaging first action potential dV/dt values from every sweep.

Action potential width

A width at a half-height of an action potential was defined as the width of the action potential. Half-height was found by calculating the middle between the highest and lowest points of an action potential. The first step in calculating mean action potential half-width of an individual neuron was to identify all action potentials on the basis of a template that was custom-made from 10-20 single spikes for each neuron. The template match factor was set to 4. All events that were found in a template search were accepted manually. A mean action potential width value for an individual neuron was estimated as an average value of all first action potential width values in every sweep.

f-I relation and gain

F-I relations (transfer functions) reveal the relationship between the injected current and the rate of action potential firing. To obtain a transfer function for an individual neuron, the magnitude of injected current for each sweep is assigned a firing rate value, which is in turn calculated from a first interspike interval (Figure 15, A). The slope of a transfer function (gain) is obtained by extracting a slope value from a linear fit of the first 3-4 points of the transfer function (Figure 15, B). To calculate gain for particular developmental stage, gain values were averaged from neurons of the same age.
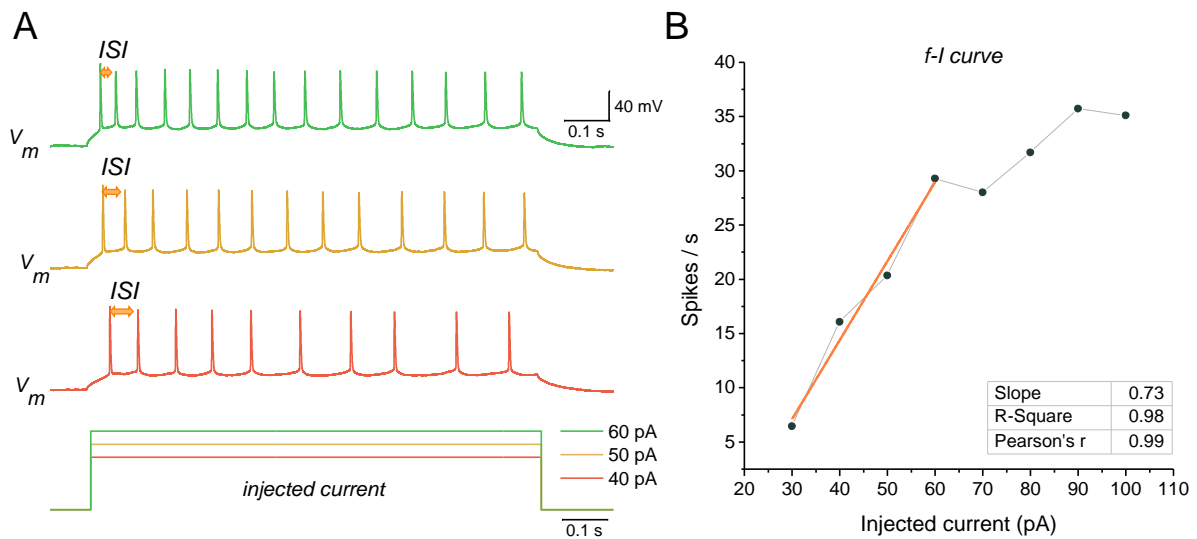
Figure 15 **Obtaining f-I relations and gains. *A*** Representative action potential trains generated in response to different magnitudes of injected current. Interspike intervals (ISI) marked in orange represent intervals that were used to calculate firing rates (spikes/s). ***B*** f-I relation of an individual neuron. Gain (the slope of the f-I relation) is calculated by fitting the first 3-4 points of the curve (orange line) and extracting the slope value from the obtained linear fit.

2.2.7. Statistics

Data distribution and correlations

For each parameter calculated, Shapiro-Wilk test of normality was utilized to test the nature of data distribution. For all normally distributed values Pearson Correlation coefficient was calculated to find possible linear relationships of these values with age; Non-normally distributed values were tested with Spearman Correlation Rank test to investigate the strength of non-linear relationships.

Comparing mean values

To compare mean values of various parameters during different postnatal developmental stages all collected events and values were pooled by age and two-tailed student's t-test was performed (EPSC interevent intervals, EPSC peak amplitudes, maximum AP upstroke and downstroke dV/dt, AP width, AP threshold, input resistance). Statistical analysis and comparison between the sexes were omitted due to a small sample size.

Biphasic graphs

For biphasic graphs, best linear fits for a part of the graph were identified for intervals with the least residual sum of squares.

Statistical analysis was conducted with *OriginPro 9.0* software. All error bars show standard error of the mean (SEM), unless specified differently. Threshold for significance levels was set at 0.05 ($p > 0.05$ = not significant = ns; $p < 0.01 - 0.05$ = significant = *; $p < 0.001 - 0.01$ = very significant = **; $p < 0.0001 - 0.001$ = extremely significant = ***).

RESULTS

The goal of this study was to analyze and to describe detailed electrophysiological profiles of the developing hippocampus in wild type male and female mice. The study can be divided into two main parts. First, we aimed to implement and to optimize an acute brain slice preparation method. It was important to select the appropriate solutions and preparatory conditions that were suitable for a wide range of developmental stages (from P5 to P22). Additionally, several technical elements for the recovery and perfusion systems had to be constructed from scratch and tuned into a well-organized and highly functional setup for robust electrophysiological recordings. The second part of the study was to evaluate both the synaptic activity and neuronal firing activity profiles in postnatally developing hippocampus. The synaptic activity was investigated to gain insight into the transformation and maturation of the synapses and tuning of hippocampal circuitry. Finally, firing activity changes were analyzed to uncover the development of the intrinsic neuronal properties that may be required for the maturation of the connectivity in the first place.

3.1. Constructing a perfusion system for electrophysiological recordings of acute brain slices

3.1.1. Constructing brain slice recovery and holding chambers

An important part of the study was to ensure that the acute brain slices were maintained healthy throughout the preparation as well as during the recording procedure. In order to save money and suit our individual needs, brain slice recovery and holding chambers were constructed from simple on-hand materials. The chambers were built to fit several criteria. First, the brain slices had to be continuously carbogenated and supplied with freely accessible aCSF (the slices had to be in direct contact with the aCSF on both sides). Secondly, the chambers had to be compartmentalized to fit brain slices by animal, sex or position in hippocampus (dorsal – medial - ventral) if needed. Lastly, the volume of the chambers had to be easily adjustable to fit the needs of different experiments.

Figure 16 shows the assembly of the recovery or holding chamber. First, inserts were constructed by cutting out the bottom of a plastic Petri dish and gluing the nylon mesh instead of it. Three inserts were then glued together. To finish the removable unit, wires were secured to the sides of the inserts. The removable unit could then be inserted into a plastic beaker of choice, and wires adjusted as needed.
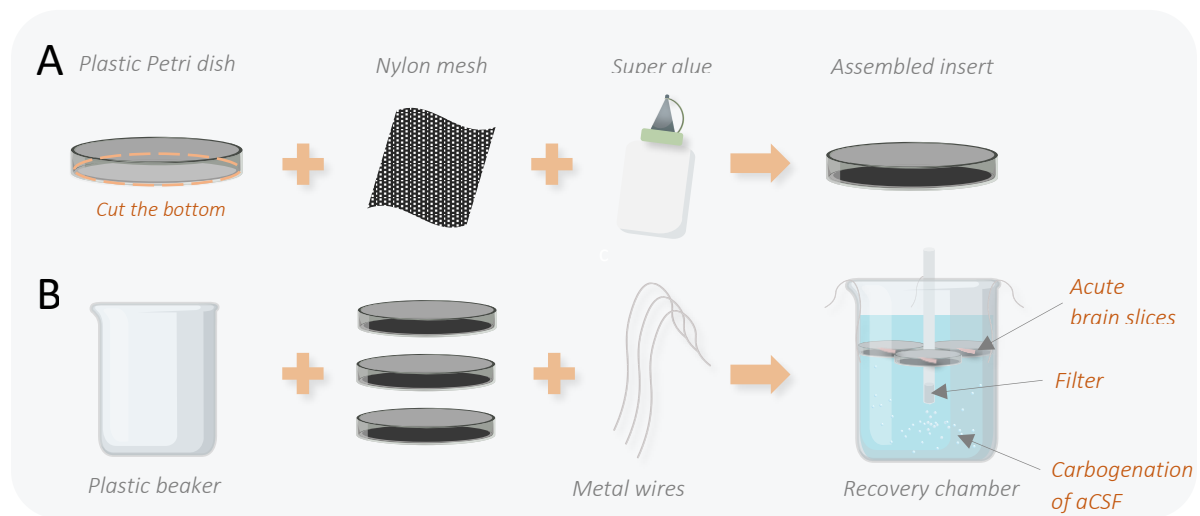
Figure 16 **The construction of the acute brain slice recovery chamber. A** The assembly of the insert started with cutting out the bottom of a plastic Petri dish. The plastic bottom was replaced by a nylon mesh that was carefully superglued to the sides of the remaining dish. **B** Three inserts were secured with one another and metal wires attached to the sides. A finished removable unit can be inserted into a beaker of choice. Illustration created by the author.

The constructed chambers had the same structure (see Figure 17), consisting of a 500 mL plastic container and a removable unit. The removable unit was composed of three individual inserts made out of Plastic Petri dishes, with a nylon mesh base layer instead of plastic bottom. Nylon mesh allowed aCSF an easy access to the slices and quick removal of the byproducts. The compartmentalization into three inserts allowed to sort the slices as needed. To ensure efficient carbogenation (95% O_2 / 5% CO_2) of aCSF and to reduce physical damage of large bubbles hitting the slices a small paper filter was inserted at the end of the gas tube to disperse the gas stream into small bubbles. The removable unit was supported with metal wires which allowed to control the height of the inserts, therefore accommodating for different volumes of aCSF.
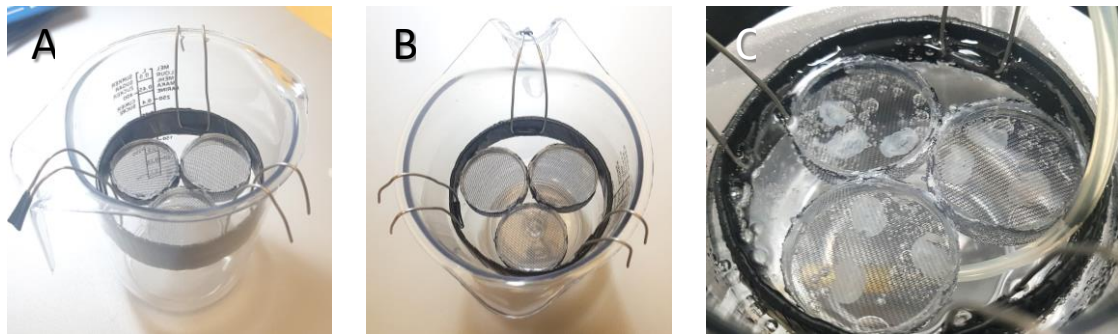
Figure 17 **The structure of the acute brain slice recovery and holding chambers. *A*** Three inserts are secured together and can be removed as a unit when needed. The shape of the attached wires can be adjusted to control height of the inserts or fit a container of choice. ***B*** View of the chamber from top ***C*** Acute brain slices submerged into constantly carbogenated aCSF and resting on top of nylon mesh inserts. The brain slices can be maintained in these conditions up to 8 hours at room temperature.

3.1.2. Designing and 3D printing a perfusion chamber

To keep acute brain slices constantly perfused during an electrophysiological recording, a custom perfusion chamber was designed and 3D printed. The perfusion chamber was modelled with AutoCAD software (see Figure 18) and 3D printed with SLA printing technology, that allowed to print particularly small details. The printing material was chosen to be a clear resin that is biocompatible, robust but pliable if adjustments are needed. The design was based on a commercial perfusion chamber model RC-26 from Warner Instruments. It has a characteristic diamond shaped bath that ensures a laminar flow of the fluid. The main bath can hold up to 200 µL of fluid at once. The main bath can also hold a 15 mm diameter round cover slip if needed. The length, width and height of the chamber are 40 mm x 23 mm x 4 mm, respectively.

The perfusion chamber was connected to the perfusion system that constantly exchanged aCSF for optimal supply of carbogen and fresh nutrients. The inlet was connected to the perfusion tubing that provided the flow of aCSF through a gravitational drip system. The fluid was collected with a help of a peristaltic pump through a coarse needle that was secured above the outlet bath. The needle could be freely moved up or down to regulate the overall height of aCSF in the chamber. A small slip was made between the main bath and the outlet bath for easing the capillary flow through the chamber. A separate agar bridge well was made for an easy access with a reference electrode.
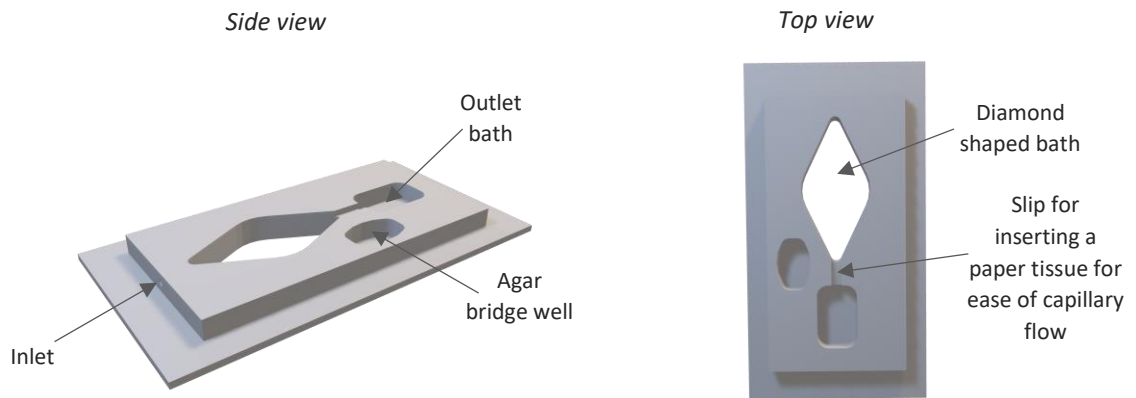
Side view　　　　　　　　　　　　　　*Top view*

Outlet bath

Diamond shaped bath

Slip for inserting a paper tissue for ease of capillary flow

Agar bridge well

Inlet

Figure 18 **A 3D model of the perfusion chamber** shown from the side and from the top

To prepare the printed perfusion chamber for use, the sides of the main bath were sanded to a 45° angle for an easier access for a recording electrode. A ramp with a needle holder was secured next to an outlet bath to insert a coarse needle when needed. To keep the perfusion chamber secure and stable throughout the experiment, the perfusion chamber was glued to a transparent plastic sheet with drilled holes that can be securely fixed with screws to the electrophysiology rig platform whenever needed (Figure 19).
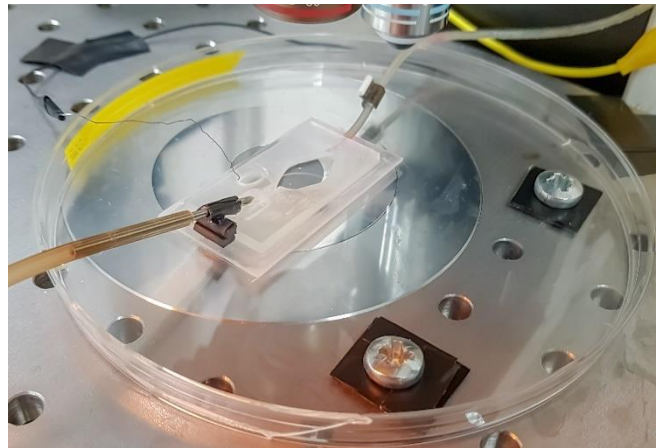

Figure 19 **A perfusion chamber** fixed to the stage. aCSF flows through the inlet tube and is collected by a fixed coarse needle, that can be moved up or down to regulate the total volume in the bath.

3.1.3. Making a brain slice anchor

To mechanically secure the brain slice during electrophysiology recording, we made a brain slice anchor. It helped to stabilize the brain slice against the flow of the aCSF. The anchor was made by bending a delicate silver wire to a shape that fitted the main bath of the perfusion chamber (see Figure 20). Individual nylon threads were then glued to the wire from the bottom side approximately 1.5 mm – 2.0 mm apart.
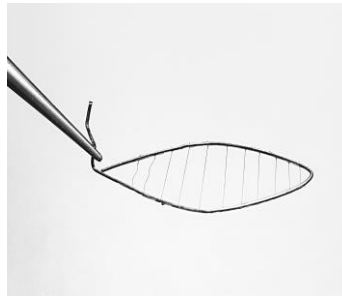
Figure 20 **A custom made brain slice anchor**

3.2.4. Assembling the perfusion system

After making separate parts for the perfusion system, they were assembled into a coherent system. The main purpose of this system was to continuously perfuse the acute brain slices with carbogenated aCSF during recovery and recording. Several different solutions could be used during the experiment (for perfusing with different drugs), regulated by three-way valves. The perfusion system consisted of a gas cylinder filled with carbogen gas (95% O_2 / 5% CO_2), a gravitational drip system, a perfusion chamber, a peristaltic pump, and brain slice recovery / holding chambers. A schematic representation of a perfusion system setup is illustrated in Figure 21:

Figure 21 **Schematic representation of the perfusion system. *A*** Carbogen gas is distributed to the brain slice recovery chambers and gravitational drip system. ***B*** A holding chamber maintains viable acute brain slices until the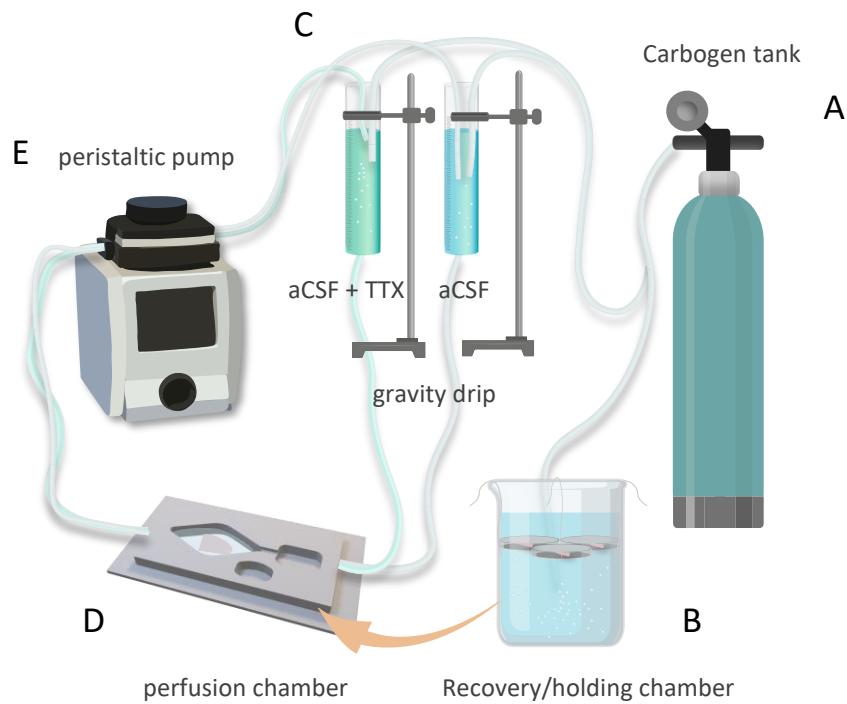 end of the experiment; peach arrow indicates the transfer from the holding chamber to the perfusion chamber for the electrophysiological recording procedure. ***C*** A gravitational drip system has two drips connected to the system that can be switched between one another if needed. ***D*** A perfusion chamber holds the acute brain slice during the electrophysiological recording; it is constantly perfused with carbogenated aCSF. ***E*** aCSF is collected from the perfusion chamber with the help of a peristaltic pump; the fluid is returned into the containers of a gravitational drip system where it is carbogenated and released back into the cycle. Illustration created by the author.

3.2. Finding a suitable cutting plane for electrophysiological recordings

A critical part in preparing acute brain slices for measuring physiological synaptic activity in hippocampal CA1 pyramidal neurons was to ensure the best preservation of major afferent hippocampal pathways, (also called trisynaptic circuit, containing the performant path, the mossy fibers and Schaffer collaterals). Having an intact neuronal activity in whole trisynaptic circuit reflects the most accurate physiological synaptic responses in electrophysiological recordings.

Initially, for reasons of convenience, we utilized transverse acute brain slices for recording synaptic activity between CA3 and CA1 hippocampal pyramidal neurons. However, the failure rate in observing

physiological synaptic activity was very high: 88.24 % of all successfully patched pyramidal neurons (15 out of 17) exhibited no or very little spontaneous synaptic activity, arguing that the cutting angle truncated neuronal arbors and obstructed synaptic transmission.

We found that the angle of brain slice sectioning is of particular importance for the preservation of long fiber pathways. Three most common slicing planes – coronal, transverse, and horizontal-entorhinal cortex (HEC), have been utilized for specific purposes in various electrophysiological studies. However, it has been shown that HEC slices may be the most suitable for studies in which all three of the major pathways must be preserved (Xiong et al., 2017). For these reasons we chose to utilize HEC slices in our study. With this cutting plane, we observed that 73.07 % of all successfully patched pyramidal neurons demonstrated typical physiological synaptic activity. HEC slices and hippocampal CA1 pyramidal neurons are illustrated in Figure 22:
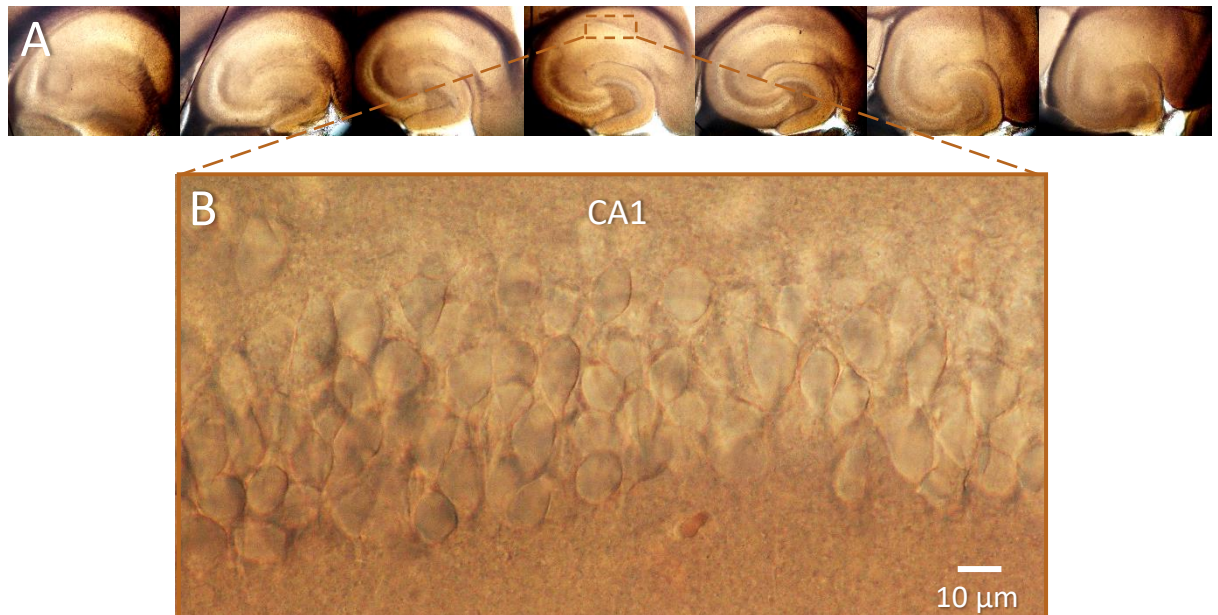

Figure 22 **A** Hippocampal HEC slices of 300 μm lined up from dorsal to ventral; Brightfield microscopy, 4x magnification. **B** Hippocampal CA1 pyramidal neuron layer; Brightfield microscopy, 40x magnification.

3.3. The postnatal development of synaptic activity in hippocampal CA1 pyramidal neurons

To evaluate the development of connectivity in hippocampal circuitry we recorded synaptic activity of individual CA1 pyramidal neurons under the voltage clamp configuration throughout the postnatal development (P5, P11, P12, P16, P18, P22). Several parameters were evaluated to characterize the synaptic transformation during development. First, to characterize synaptic connectivity between CA3 – CA1 neuron pairs we evaluated the duration of interevent intervals of recorded EPSCs. Second, to characterize synaptic strength, peak amplitudes of EPSCs were measured. Finally, to gain some insight into the efficacy of synaptic transmission we evaluated synaptic multiplicity at postnatal day 16.

3.3.1. EPSC interevent intervals during postnatal development

To estimate synaptic connectivity between CA3 – CA1 pyramidal neurons during development we characterized interevent intervals of recorded EPSCs. Figure 23, A illustrates sample sweeps of synaptic activity during postnatal days 5, 12 and 22, demonstrating that the rate of occurrence of synaptic events increased during development. It was also noticeable that the apparent amplitude of the recorded EPSCs was higher in magnitude with age. All of the interevent intervals of EPSCs were then pooled by age and cumulative probabilities graphed to evaluate the distribution of these events during development. Figure 23, B demonstrates that there was a steady decrease in the duration of interevent intervals with age. Mean interevent interval values dropped four-fold from 0.826 s $\pm$ 0.017 s at P5 (n=4) to 0.204 s $\pm$ 0.002 s at P22 (n=2), ***p=2.02E-244 (Figure 23, C). Regression analysis of mean EPSC interevent intervals of individual neurons during development suggested a significant negative linear relationship; Pearson Correlation coefficient was -0.670** (p=1.70E-3, n=19). Graphs demonstrating values of individual neurons are illustrated in Figure S1. The increase of the occurrence of the synaptic events suggested that synaptic contacts between pairs of CA3 – CA1 neurons steadily increased with age.
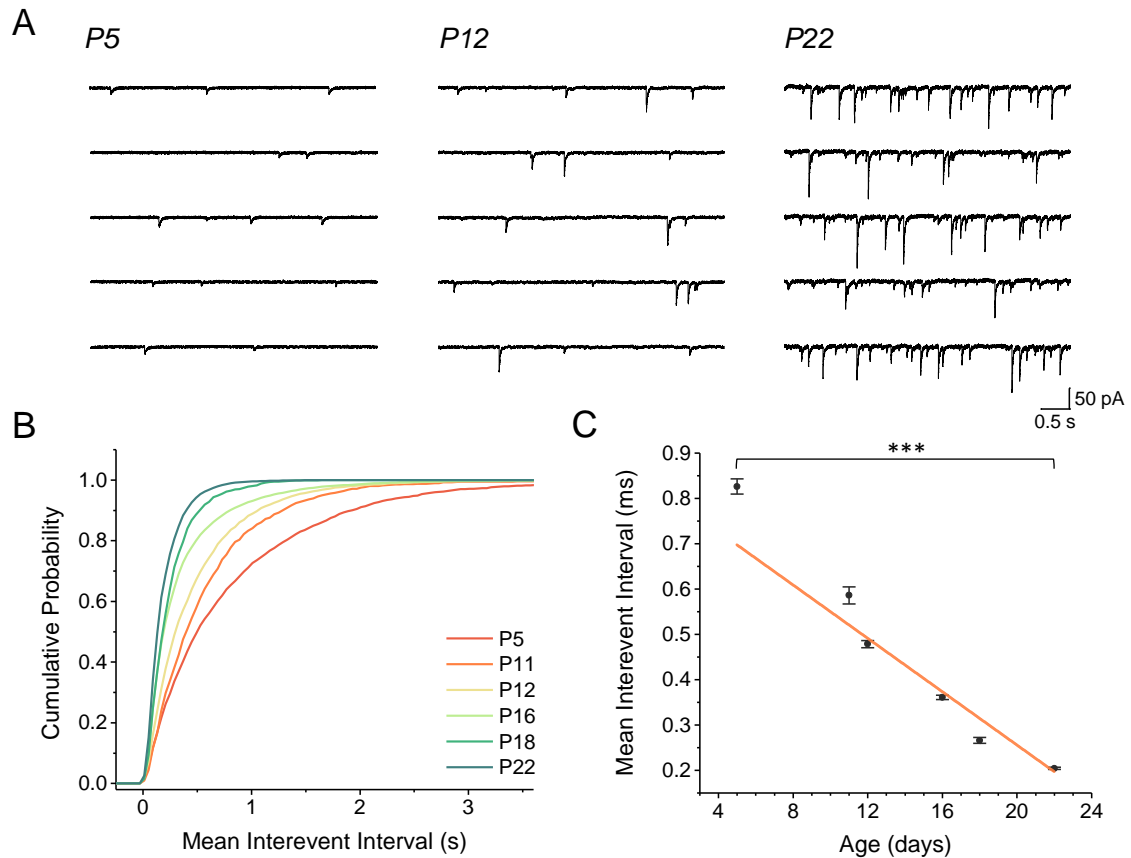
Figure 23 **EPSC Interevent Intervals during postnatal development.** *A* Sample sweeps of physiological synaptic activity recorded in CA1 pyramidal neurons during different postnatal ages. *B* Cumulative probability graphs indicate that the duration of interevent intervals was getting shorter with age; *C* Mean EPSC interevent interval values decrease significantly from P5 to P22, ***p=2.02E-244. Mean values were calculated by pooling interevent intervals from individual neurons by age (P5(n=4); P11(n=2); P12(n=3); P16(n=7); P18(n=1); P22(n=2)); Data are presented as a mean $\pm$ SEM; Orange line indicates a linear fit.

3.3.2. Peak amplitudes of EPSCs during postnatal development

To characterize synaptic strength, peak amplitudes of EPSCs were evaluated throughout the postnatal development. Figure 24, A shows averaged traces of EPSCs and their derivative functions at postnatal days 5, 16 and 22. The amplitude of EPSCs increased with age. Cumulative probability graphs indicate that more events had larger amplitude at the later stages of development when compared to younger animals (Figure 24, B). Unlike the gradual change in interevent intervals during development, peak amplitudes of EPSCs followed a biphasic trend (Figure 24, C): mean values were stable for the first two weeks of postnatal development (8.02 $\pm$ 0.09 pA at P5 (n=4); 8.58 $\pm$ 0.34 pA at P11 (n=2) and 7.88 $\pm$ 0.11 pA at P12 (n=3)) and increased the following week from 8.56 $\pm$ 0.06 pA at P16 (n=7) to 14.78 $\pm$

0.25 pA at P22 (n=2), ***p=1.08E-118. To see whether a latent increase in amplitude was linearly correlated with age, Pearson correlation coefficient was calculated for the interval between ages of P16 and P22 (Pearson's r: 0.59; p=0.07; n=10). Graphs demonstrating values of individual neurons are illustrated in Figure S2. These results suggested that synaptic strength remained constant during the first couple of weeks of postnatal development and increased during the third week after birth.
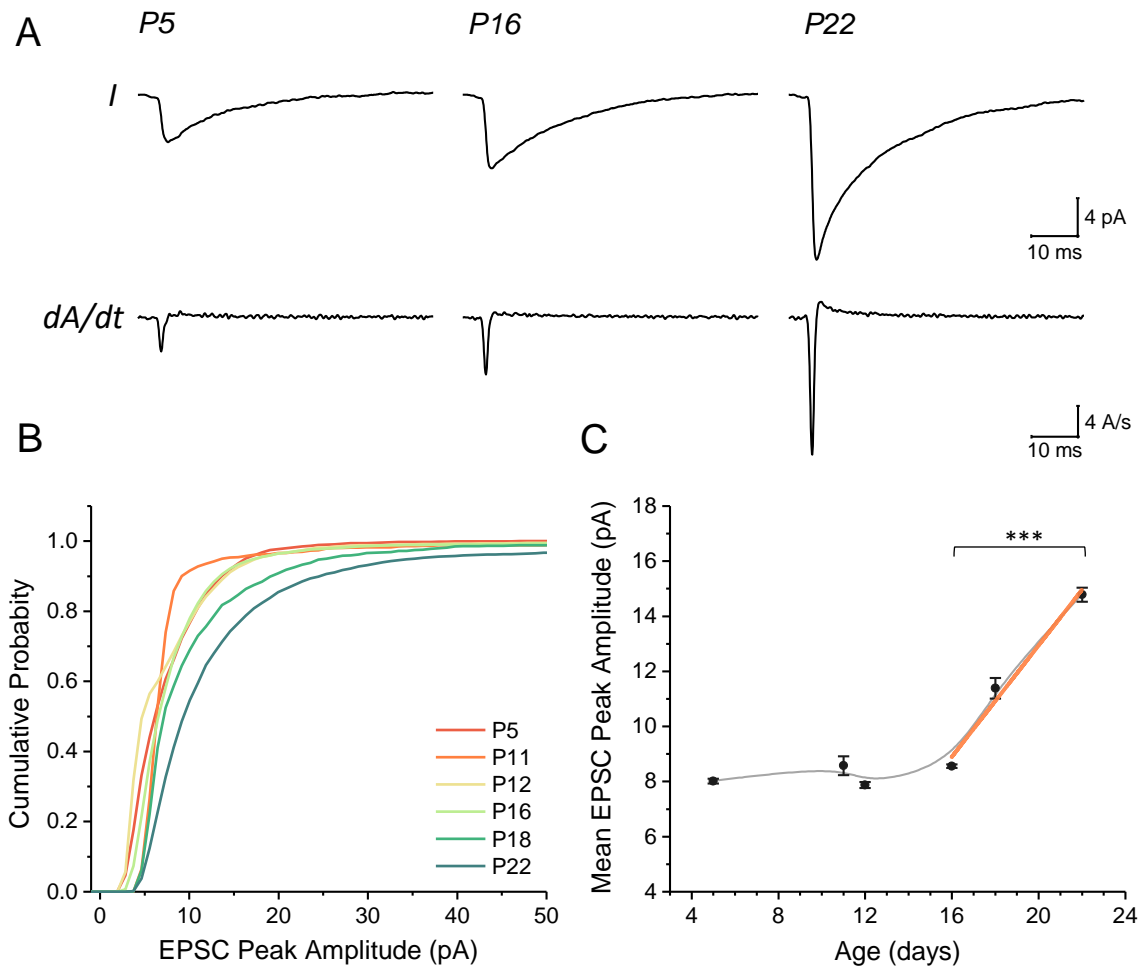
Figure 24 **Peak EPSC amplitudes during postnatal development.** *A* Representative EPSC traces and their derivative functions at different stages of postnatal development. Each trace was averaged from all EPSC events recorded in a 10-minute voltage clamp recording while neuron was clamped at resting potential (-70 mV). *B* Cumulative probability graphs indicate that an increasing part of EPSC events is higher in amplitude with age. *C* Mean EPSC peak amplitudes increase significantly from P16 to P22, ***p=1.08E-118. All events from individual neurons were pooled by age to calculate mean EPSC peak amplitudes (P5(n=4); P11(n=2); P12(n=3); P16(n=7); P18(n=1); P22(n=2)); Data are presented as a mean ± SEM; Orange line indicates linear fit; Values are connected with a B-spline (gray line) for visual clarity.

3.3.3. Synaptic multiplicity and quantal size at P16

To characterize the efficacy of synaptic transmission, we evaluated synaptic multiplicity at postnatal day 16. Synaptic multiplicity can be defined as an average number of functional synapses between pairs of neurons under investigation and is a good indicator of the effectiveness of synaptic transmission (Albert Y. Hsia et al., 1998). Figure 25, A shows sample sweeps of recorded EPSCs before and after the application of 0.5 µM TTX. The presented fragments of the recording suggested that that the apparent amplitudes of EPSCs were smaller and the occurrence of the events was less frequent after the application of TTX, indicating that the multiplicity value in this experiment was larger than one (the average number of synapses between a pair of CA3-CA1 neurons was more than one). Cumulative probability graphs for the EPSC interevent intervals (Figure 25, B) indicate that more events were longer in duration after applying TTX. Figure 25, C shows that mean values of interevent intervals increased approximately two times after perfusing with TTX (0.223 ± 0.003 s before TTX (n=2) and 0.469 ± 0.009 s after TTX (n=2); ***p=1.64E-114).

Together with a change in frequency of the events, a change in amplitudes of the EPSCs was evaluated. Figure 25, D shows averaged traces of EPSCs before and after applying TTX. More EPSCs were smaller in amplitude after TTX application (Figure 25, E) and a mean amplitude value decreased from 9.20 ± 0.09 pA (n=2) to 5.30 ± 0.04 pA (n=2), ***p=3.24E-203 (Figure 25, F). To verify that the recorded activity was consistent throughout the experiment, we plotted the distributions of recorded amplitudes in time. The graphs indicated that the recorded events and their amplitudes were distributed homogenously throughout the duration of the experiment (Figure 25, G). This meant that the recorded values were driven by normal physiological activity and were not shifted by inconsistent or burst-like activity.

The mean amplitude of the miniature excitatory currents (EPSCs recorded in presence of TTX) is considered to be an estimate of a mean quantal size (q). Mean quantal size represents a current in response to neurotransmitters released from a single presynaptic vesicle and remains relatively constant throughout development. Consistent with other studies, the mean quantal size in this experiment was calculated to be 5.30 ± 0.04 pA (n=2). From the parameter values obtained in this experiment, mean multiplicity value was calculated to be 1.94 ± 0.13 (n=2), which is well in accordance with values for hippocampal CA1 pyramidal neurons in rats at P16 (Albert Y. Hsia et al., 1998; Paolicelli et al., 2011).
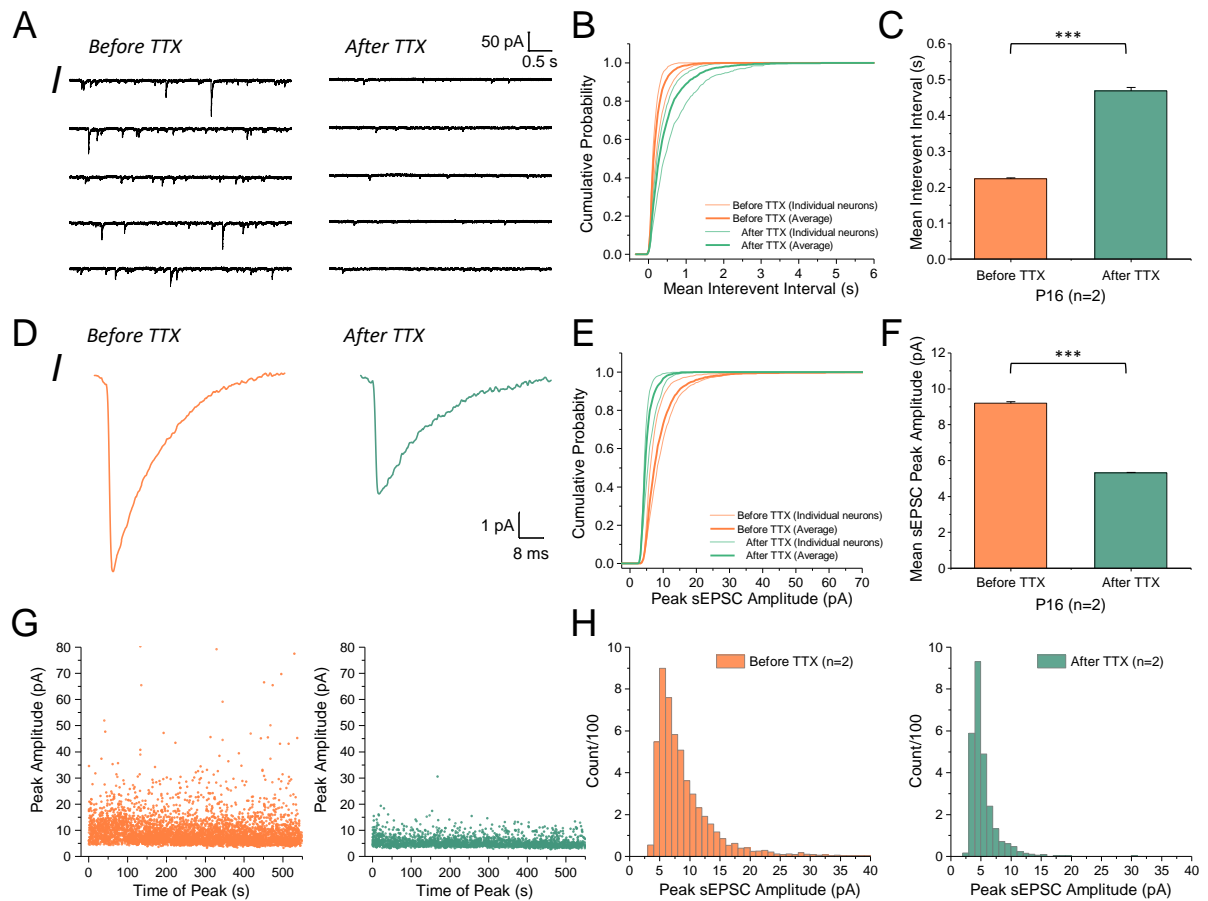
Figure 25 **Synaptic multiplicity at P16. *A*** Sample sweeps illustrating the effect of 0.5 µM tetrodotoxin (TTX) on spontaneous activity of CA1 pyramidal neurons at P16. Application of TTX reveals miniature EPSCs that represent action potential independent neuronal activity. At this age, TTX reduced the amplitude and frequency of recorded events by a half. *B* Cumulative probability graph of EPSC interevent intervals before and after applying TTX. Thin lines show cumulative probabilities of individual neurons, while thicker line indicates averaged probabilities (n=2). *C* Mean duration of EPSC interevent interval increases after applying TTX (n=2, ***p=1.64E-114). Data are presented as a mean ± SEM; *D* Average traces of excitatory postsynaptic currents before and after applying TTX (n=2). *E* Cumulative probability graph of EPSC peak amplitudes. Thin lines show cumulative probabilities of individual neurons, while thicker line indicated averaged probabilities (n=2). *F* Mean EPSC peak amplitude decreases after application of TTX. Data are presented as a mean ± SEM; ***p=3.24E-203; *G* The distribution of recorded events and their amplitudes in time. These graphs indicate a stable and homogenous neuronal activity in time before (left) and after (right) applying TTX and show that the calculated mean values are not shifted by burst-like activity. *H* Peak amplitude distribution histograms of recorded sEPSC (before TTX) and mEPSC (after TTX) events. A width of peak EPSC amplitude distribution at P16 is about two times larger before applying TTX, suggesting that the contribution of action potential dependent activity is approximately two times larger than action-potential independent release at P16.

3.4. The postnatal development of intrinsic firing properties of hippocampal CA1 pyramidal neurons

In rodents, a substantial amount of hippocampal development occurs during the first postnatal month (I. Spigelman et al., 1992). Therefore, it is valuable to characterize membrane excitability and firing properties during this developmental period to understand how it impacts the formation of complex neuronal circuits. In this study we evaluated multiple intrinsic firing properties of hippocampal CA1 pyramidal neurons under the current clamp configuration throughout postnatal development (P5, P11, P12, P16, P18, P22).

3.4.1. Spike characteristics during postnatal development

First, we evaluated action potential properties during postnatal development. The intracellular injection of depolarizing current of sufficient strength evoked single or multiple action potentials in all neurons throughout the development. Figure 26, A illustrates representative action potentials and their corresponding derivatives at postnatal days 5, 12 and 22. The apparent amplitude of action potentials increased with age, whereas width progressively decreased. First, we characterized the depolarization and repolarization speeds of first action potentials in recorded spike trains in response to injected current pulses of one second (Figure 26, B-C): mean maximum action potential upstroke dV/dt values increased about four-fold from 45.04 ± 2.58 V/s at P5 (n=3) to 167.66 ± 2.01 V/s at P22 (n=1), ***p=1.08E-22; A positive linear relationship, although not significant, was revealed with Pearson correlation between ages P5 and P22 (Pearson's r: 0.39; p=0.16; n=14). Concurrently, maximum downstroke dV/dt values decreased around three times from -10.25 ± 0.40 V/s at P5 (n=3) to -33.53 ± 0.51 V/s at P22 (n=1). The largest and significant decrease in these values was from P5 to P12, ***p=6.11E-33. Pearson correlation for this interval was -0.79**; p=0.01; n=9.

Second, we evaluated the width of the first action potential in a spike train (measured at a half height of an action potential), Figure 26, B. The width of an action potential was longest in immature neurons at P5 (12.83 ± 0.91 ms; n=3); then decreased significantly during the following week (2.96 ± 0.24 ms at P12; n=5), ***p=1.47E-10; and stayed relatively similar for the next 10 days (4.83 ± 0.38 ms at P16 (n=4) and 3.43 ± 0.29 ms at P22 (n=1)). A significant negative linear relationship between action potential width and age was revealed with Pearson correlation between ages P5 to P12 (Pearson's r: -0.98***; p=4.21E-6; n=9). Finally, mean action potential threshold values were obtained from first action potentials in a spike train (Figure 26, C): the mean threshold decreased from -38.64 ± 0.53 mV at P5 (n=3) to -55.26 ± 0.19 mV at P22 (n=1)), ***p=4.75E-19. Pearson correlation showed a linear

negative relationship between threshold and age: -0.43 (p=0.12; n=14). Graphs demonstrating values of individual neurons are illustrated in Figure S4. Additionally, we created developmental profiles of intrinsic firing properties; representative profiles are illustrated in Figure S6.

These developmental changes in action potential parameters could be linked to a quantitative increase of ion channel incorporation into the membranes of pyramidal neurons, with Na^+ channels affecting the rising phase of the spike and K^+ channels contributing to the falling phase of the spike.
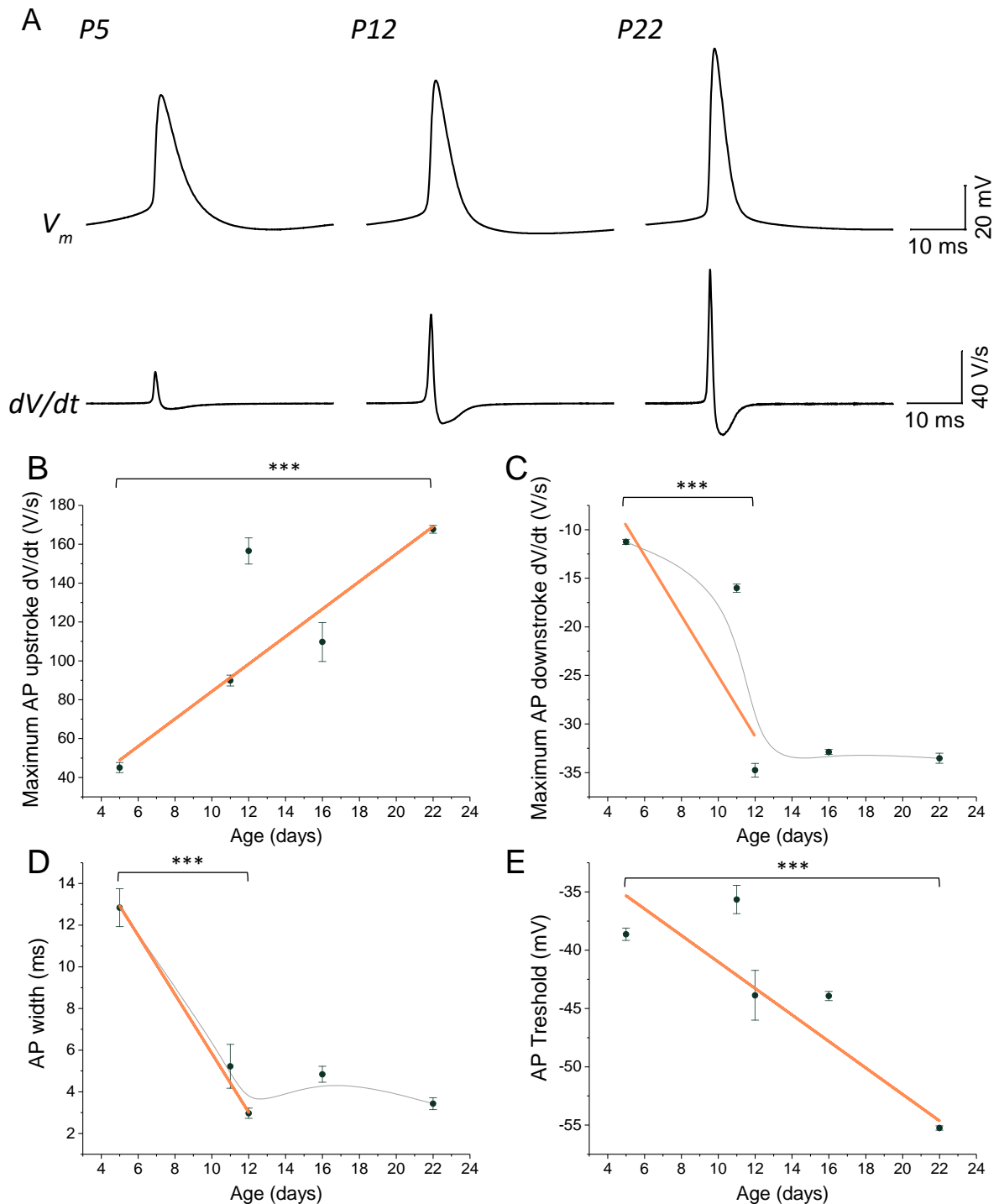
Figure 26 **Action potential characteristics during development.** *A* Representative action potentials and their corresponding derivative traces at different stages of postnatal development. Each trace is averaged from action potentials from one or more neurons at each age (P5(n=3); P12(n=5); P22 (n=1)). *B* Maximum action potential upstroke derivative values increased significantly from P5 to P22, ***p=1.08E-22. Data are presented as a mean $\pm$ SEM; Orange line indicates linear fit. *C* Maximum action potential downstroke derivative values decrease with age. Largest reduction in values was from P5 to P12, ***p=6.11E-33. Orange line indicates linear fit. Data are presented as a mean $\pm$ SEM; *D* Mean action potential width values during development dropped significantly from P5 to P12, ***p=1.47E-10. Action potential width values were calculated by measuring width at the middle of the highest and the lowest points of an action potential. Orange line indicates linear fit. Data are presented as a mean $\pm$ SEM; *E* Mean action potential threshold values decrease significantly from P5 to P22, ***p=4.75E-19. Data are presented as a mean $\pm$ SEM; Values in C and D are connected with a B-spline (gray line) for visual clarity. Number of neurons analyzed in B, C, D and E: P5(n=3); P11(n=1); P12(n=5); P16(n=4); P22 (n=1).

3.4.2. Input resistance during postnatal development

Second, we obtained input resistance (R_{in}) values throughout postnatal development. We found that R_{in} of hippocampal pyramidal neurons decreased substantially during postnatal development (Figure 27). The largest decrease in average R_{in} values was observed from P5 (2293 $\pm$ 273 MΩ; n=6) to P11 (314 $\pm$ 141 MΩ; n=3), ***p=6.39E-4; R_{in} values reached a plateau by approximately P16. Pearson correlation for this age interval suggested a significant negative linear relationship (Pearson's r: -0.92***; p=3.52E-6; n=14). Graphs demonstrating values of individual neurons are illustrated in Figure S3. A large decrease in R_{in} values suggests large changes in neuronal membrane composition, that could be attributed to incorporation of different ion channels and an increase in surface area of neuronal membrane.
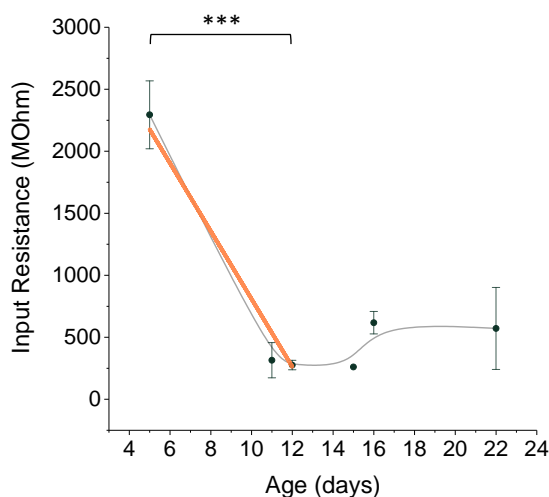

Figure 27 **Input resistance during postnatal development.** Mean Input resistance values decrease with age (P5(n=6); P11(n=3); P12(n=5); P16(n=6); P22 (n=2)). A significant drop in values is observed from P5 to P12, ***p=6.39E-4. Data are presented as a mean $\pm$ SEM; Orange line indicates linear fit. Values are connected with a B-spline (gray line) for visual clarity.

3.4.3. f-I relation and gain during postnatal development

Finally, we evaluated persistent firing properties of developing neurons. During current clamp recordings we observed that immature neuronal cells had lower range of firing frequencies in response to the intracellular injections of depolarizing current compared to more mature neurons. For example, the highest number of spikes in response to one second depolarizing current reached about 9 at P5 (n=3), whereas at P12 the pyramidal cells were capable of firing on average 20 spikes per second (n=5). To compare how firing rates were affected by the magnitude of the injected current we plotted f-I relationship curves for individual neurons throughout the development (Figure S5). Gain (the slope of the f-I curve) was obtained by fitting the starting linear phase of each of the transfer functions (Figure 28, A). We found that the mean gain stayed relatively constant during the first 12 days of postnatal development and then rapidly increased by more than three-fold from 0.19 ± 0.02 at P12 (n=5) to 0.72 ± 0.07 at P22 (n=1) (Figure 28, B); Pearson correlation for this interval indicated a significant linear relationship: Pearson's r: 0.91***; p=2.96E-4, n=10; Larger gains in more mature neurons could indicate a better ability to sustain persistent firing activity.

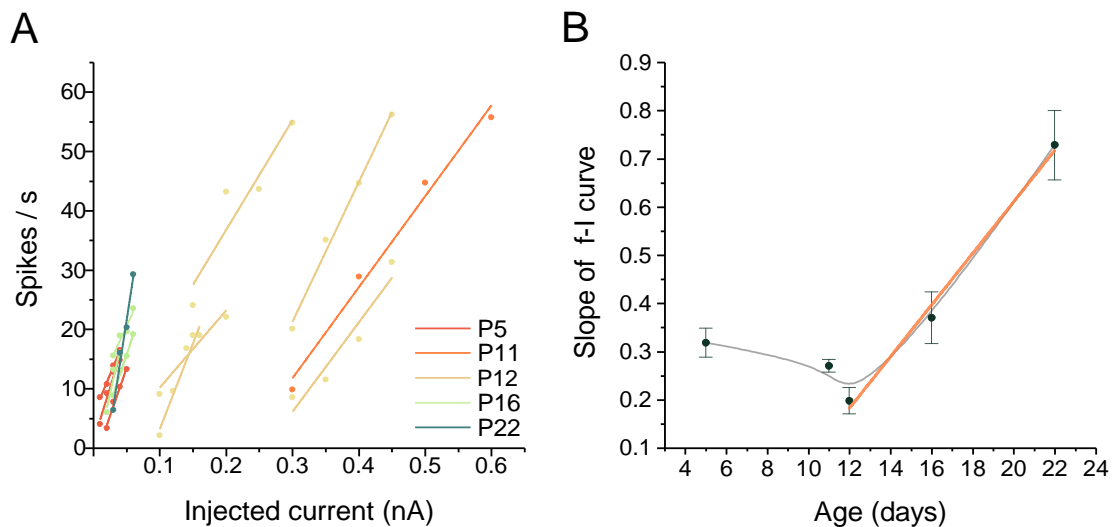*Figure 28* **f-I relation and gain during postnatal development.** *A* Linear fit of the f-I relations: the fitted functions were generated from the initial linear phases of the f-I curves (first 3-4 points). *C* Mean gains (the slope of the linear fit of the f-I curve) increase with age. Data are presented as a mean $\pm$ SEM; Orange line indicates linear fit. Values are connected with a B-spline (gray line) for visual clarity.

3.4.4. Firing frequency adaptation during postnatal development

Additionally, we investigated whether action potential trains recorded in response to injected current showed firing adaptation depending on the age of postnatal development. Pyramidal neurons of all postnatal ages demonstrated firing frequency to some extent (Figure 29). The lowest firing frequency adaptation values were observed in most juvenile neurons (0.0098 ± 0.0007 at P5 (n=3)). Although there was no clear trend seen from the data, Spearman correlation coefficient indicated a significant non-linear relationship between age and firing frequency adaptation values (Spearman Corr: 0.89; p=0.04; n=14). These results indicate that more mature neurons have better firing frequency adaptation that might be related to gradual incorporation of ion channels responsible for such mechanisms. A large frequency adaptation value at P11 might indicate a transient adaptation mechanism as a compensation for transitions in ion channel density and/or subunit composition; alternatively, it could be an outlier and more neurons need to be investigated to make stronger arguments.
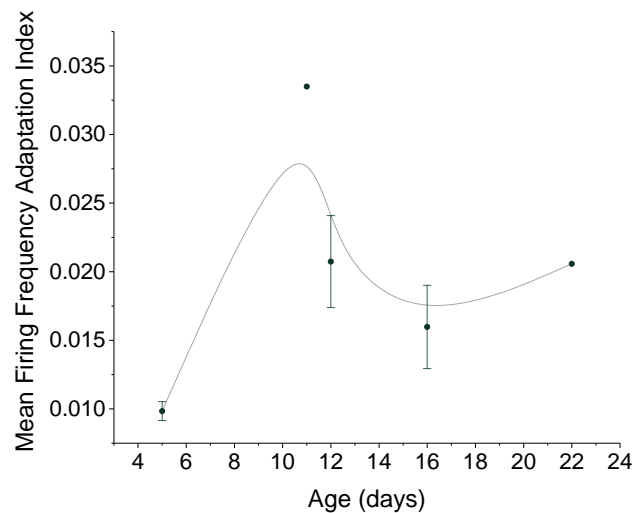

Figure 29 **Mean firing frequency adaptation during postnatal development.** Lowest adaptation values were observed in most juvenile neurons. Data are presented as a mean $\pm$ SEM: P5(n=3); P11(n=1); P12(n=5); P16(n=4); P22 (n=1); Values are connected with a B-spline (gray line) for visual clarity.

DISCUSSION

4.1. Synaptic activity and strength throughout postnatal development

Anatomical and immunohistochemical studies suggest that the number of synapses between the pairs of CA3 – CA1 pyramidal neurons increases during postnatal development (Harris,' et al., 1992; Paolicelli et al., 2011). Whether observed neonatally formed synapses reflect increasing functional connectivity can be determined by analyzing electrophysiological profiles of synaptic activity throughout postnatal development. We found that the interevent intervals of recorded EPSCs steadily decreased four-fold from P5 to P22 (Figure 23). Simultaneously, the amplitudes of EPSCs stayed relatively constant from P5 to P12 and then increased from P12 to P22 (Figure 24). The positive shift in EPSC event frequency and amplitude could be associated with several different quantal parameters of synaptic transmission, including increased probability of neurotransmitter release (P_r), increased quantal size (q) or increased number of functional synapses (n). Interestingly, no developmental change was observed in either release probability or quantal size during the postnatal development of hippocampal pyramidal neurons in rats (Albert Y. Hsia et al., 1998). Hence, the developmental increase of EPSC event frequency and amplitude observed in this experiment could possibly be attributed to the increase of functional CA3 – CA1 synapses. Additionally, a change in frequency of the synaptic events can also in part be a result of an increased activity of the neuronal network.

4.2. Synaptic multiplicity during neonatal development

We observed that the increase in frequency and amplitude of recorded EPSCs followed distinct timelines: the frequency steadily increased from P5 to P22, while the amplitude had a latency period with the increase starting only at P12 (Figure 23 and Figure 24). One possible reason for this disparity of the timelines might be explained by a change in multiplicity during postnatal development (Figure 25). During the first couple of weeks after birth, synaptic contacts might have been made and new pyramidal CA3 – CA1 neuron pairs that had not had contacts before might have been formed. Because of the increasing number of new neuronal pairs, we observed an increase in EPSC frequency. However, because there was only one contact between each pair, the recorded amplitudes of EPSCs were still the same, as there was no possibility of temporal summation from synchronous release of vesicles from multiple synapses (i.e., multiplicity value was equal to one). The observed EPSC amplitude started

to increase when additional synapses started to form between individual CA3 – CA1 neuron pairs (multiplicity value increased). Hsia et al. (1998) reported the change of multiplicity values over postnatal development in rat hippocampal CA1 pyramidal neurons. During the first two weeks after birth, multiplicity values were equal to 1.0 and increased slowly to reach values of 1.15. During the following several days, the multiplicity values increased rapidly to 1.5 and then reached 2.10 in mature adults. The multiplicity value that we defined at P16 was 1.94, thus coinciding with the reported values of Hsia et al. (1998) study. The biphasic change of synaptic multiplicity could explain the latent growth of EPSC amplitudes that we characterized in our experiments.

A large contribution to the reorganization of the synapses and an increasing multiplicity during postnatal development of hippocampal neurons could be attributed to microglial activity. Recent studies have demonstrated that microglia plays an important role in the formation, elimination and maturation of synapses in the developing brain (Miyamoto et al., 2016; Paolicelli et al., 2011; Parkhurst et al., 2013; Schafer et al., 2012; Sipe et al., 2016; Zhan et al., 2014). In one immunohistochemical study, microglial volume and phagocytic capacity (parameters that could associated with synaptic pruning, (Schafer et al., 2012)) have been evaluated throughout the critical stages of postnatal development (Weinhard et al., 2018b). The greatest values are reached at P15, consistent with our observed increase of EPSCs starting from P12. But how could microglia be linked with an increase in synaptic multiplicity? A compelling argument for this matter is reported by (Weinhard et al., 2018a). A time-lapse imaging data has revealed that upon the contact of microglia, a transient spine head filopodia is induced. The induction is frequently followed by a relocation of the spine head to the tip of the filopodium and occasionally resulting in a new contact with a bouton. Interestingly, spine switching has been shown to rearrange single-synapse boutons into multisynaptic boutons (MSBs) (Geinisman et al., 2001; Richards et al., 2005). If the spines of the MSBs are on the same dendrite, these MSBs are characterized as class I MSBs. Conversely, if the spines of the MSB are from separate dendrites, they are defined as class II MSBs. Class I MSBs are reported to increase during postnatal development and facilitate the strengthening of excitatory connectivity (Zhan et al., 2014). An increase in class I MSBs mediated by microglia could explain the increased synchronous release of presynaptic vesicles in response to an AP, thus observing larger apparent EPSCs and increased multiplicity.

4.3. The postnatal development of intrinsic firing properties

It has been reported, that microglia-mediated synaptic shaping is a process dependent on neuronal activity (Schafer et al., 2012). In turn, developmental neuronal activity is highly dynamic and is largely influenced by kinetic characteristics, density and composition of diverse membrane ion channels (Moody and Bosma, 2005). We found that intrinsic neuronal characteristics and firing properties of

hippocampal CA1 pyramidal neurons transformed substantially during postnatal development. We showed that action potentials in CA1 neurons grew in amplitude and decreased in duration with age (Figure 26, A), which is consistent with studies conducted in rat hippocampal slices (Sánchez-Alonso et al., 2012; I. Spigelman et al., 1992). Concurrently, we observed a progressive increase in the rate of both the rising and falling phases of the action potential (Figure 26, B-C), which could be associated with postnatal changes in the kinetics and density of ionic channels that underlie genesis and repolarization of an action potential. More specifically, the increasing rate of the rising phase of an action potential is related to membrane conductance to Na^+ (Hondeghem, 1978; Strichartz and Cohen, 1978), while the falling phase has been shown to be mainly dependent on K^+ currents (I. Spigelman et al., 1992). There is a general pattern of a marked increase in Na^+ and K^+ channel and current density up to three weeks of postnatal development in cortical and hippocampal pyramidal neurons (Couraud et al., 1986; Falk et al., 2003; Guan et al., 2011; Picken Bahrey and Moody, 2003). Curiously, we observed that while the increase in depolarization speed was consistently progressive throughout the postnatal development, the repolarization speed dropped from P5 to P12 and remained considerably consistent further in development. That suggests that incorporation of sodium and potassium ion channels has distinct timelines. Moreover, action potential width seemed to follow a very similar developmental pattern to repolarization values (a substantial decrease from P5 to P12 and stabilizing further in development, (Figure 26, D)), arguing that the width of an action potential might partly depend on potassium ion channel incorporation into the neuronal membrane. Interestingly, spike repolarization in immature rat hippocampal CA1 neurons is mainly dependent on the transient K^+ current, whereas more mature neurons have developed a variety of sustained K^+ currents; a mechanism that allows for a better control of action potential repolarization and repetitive discharge (I. Spigelman et al., 1992).

Consistent with our findings (Figure 26, E), action potential threshold decreases during development (McCormick and Prince, 1987; Picken Bahrey and Moody, 2003; Zhang, 2004). It has been shown that Kv1-mediated currents are major contributors to spike threshold in mature pyramidal cells (Guan et al., 2007) and grow in amplitude in pyramidal neurons during development (Guan et al., 2011).

We also found that the repetitive firing behavior changed with age in hippocampal CA1 pyramidal neurons: immature neurons could sustain a more limited range of firing frequencies than their more mature counterparts. Additionally, slopes of f-I relationships increased during postnatal development (Figure 28). Both Kv1 and Kv2 mediated currents increase during postnatal development in pyramidal neurons (Guan et al., 2011) and are shown to regulate interspike intervals in cortical pyramidal cells (Guan et al., 2007; Liu and Bean, 2014).

Additionally, we showed that input resistance decreased 7-fold during the first 12 days of postnatal development (Figure 27). Such changes have been reported in hippocampal and cortical pyramidal

neurons in rodents (Christophe et al., 2005; Lorenzon and Foehring, 1993; McCormick and Prince, 1987; Oswald and Reyes, 2008; Picken Bahrey and Moody, 2003). Interestingly, R_{in} values of mouse neocortex neurons showed little change from E16 to P2 (Picken Bahrey and Moody, 2003), arguing that the rapid development of intrinsic membrane properties starts after birth. A dramatic change in R_{in} could be attributed to an increasing size of the soma and extensive arborization of dendritic processes as well as to a progressive decrease in a specific membrane resistivity, that may be the consequence of the increases in ionic channel density discussed above (McCormick and Prince, 1987). A combination of a compact size and large input resistance of immature CA1 neurons likely contributes to the high degree of observed excitability, so that even relatively small membrane conductance fluctuations can trigger significant voltage responses. It is possible that these conditions are a developmental compensation mechanism for the relatively immature synaptic inputs to CA1 in newborn animals (Michelson and Lothman, 1989; Schwartzkroin, 1981; I. Spigelman et al., 1992).

4.4. A proposed model for postnatal development of hippocampal circuitry

A study with transgenic mice with reduced excitability of CA1 pyramidal neurons found that silenced neurons show altered spine development and synaptic transmission after postnatal day 15 (Johnson-Venkatesh et al., 2015). Interestingly, a typical developmental increase in spine density between P6 to P11 was unaltered by the suppression of neuronal excitability. Thus, intrinsic excitability of CA1 pyramidal neurons does not seem to be crucial for initial spine formation but plays an important role in expanding synaptic connectivity at later developmental stages (Johnson-Venkatesh et al., 2015). These findings coincide with the developmental timelines for the maturation of intrinsic excitability and synaptic transmission that we found in our study. In the light of our findings and those published by others, we propose a simple developmental model of maturation of hippocampal neurons. During the first two weeks of postnatal development, an abundance of new synapses forms between CA3 – CA1 pyramidal neurons. At this time, the generation of neonatal synapses is independent of neuronal activity. Simultaneously, hippocampal CA1 pyramidal neurons undergo substantial changes in intrinsic membrane properties, that could be largely attributed to the increase in neuronal size, arborization, and incorporation of diverse membrane channels. Consequently, the change of intrinsic properties leads to a transformation of neuronal firing activity, which initiates activity-dependent and microglia-mediated synaptic reorganization and strengthening of select hippocampal circuitry.

4.5. Limitations and future directions

A major limitation of this study is a small sample size of the recorded neurons. An initial goal of comparing the electrophysiological developmental profiles between the sexes was not possible due to this cause. Additionally, multiplicity values were obtained at P16 only. Even though our data was consistent with the findings in rats, we are planning to increase our sample size and to obtain multiplicity values at different stages of postnatal development in mice to strengthen the validity of the arguments presented this study. Moreover, the experiments characterizing AMPA and NMDA mediated currents will be carried out to help understand the role of silent synapses in the development of hippocampal circuitry. Nevertheless, the acquired data serves as a great insight into the development of synaptic activity and intrinsic firing properties in hippocampal CA1 pyramidal neurons in mice. With increased sample size it will serve as a solid baseline for future studies that will help to advance the knowledge of mechanisms underlying brain development in health and disease.

CONLUSIONS

Using a variety of electrophysiological techniques, we evaluated the synaptic activity and intrinsic firing properties of hippocampal CA1 pyramidal neurons in mice during various stages of postnatal development. To accomplish that, we first implemented and optimized a method for the preparation, maintenance and robust recordings of acute brain slices. We found that:

1. Synaptic activity and strength increased during postnatal development. Progressive increase of the frequency of recorded synaptic events started a week earlier than that of the amplitude.
2. Action potentials increased in amplitude, decreased in duration, and had more rapid rising and falling phases during postnatal development. Concurrently, the values of action potential threshold decreased.
3. Input resistance decreased during postnatal development. During maturation, the f-I relationships became steeper and neurons acquired a larger range of firing frequencies.

Our data supports that both intrinsic firing properties and synaptic activity change extensively during postnatal development and are critical for development of characteristic hippocampal circuitry. More studies are needed to pinpoint the exact mechanisms through which they shape one another to reach neuronal maturity.

VILNIUS UNIVERSITY

LIFE SCIENCES CENTER

INSTITUTE OF BIOSCIENCES

Kornelija Vitkutė

Master thesis

INTRINSIC FIRING PROPERTIES AND SYNAPTIC ACTIVITY OF MOUSE HIPPOCAMPAL PYRAMIDAL NEURONS DURING POSTNATAL DEVELOPMENT

SUMMARY

In hippocampus, postnatal development is a critical period for neuronal maturation and for the organization of neural pathways. At this time, neonatal pyramidal neurons grow in size and transform extensively in terms of the composition and the kinetic properties of membrane ion channels, leading to a gradual maturation of coherent and cell-type specific neuronal activity. Simultaneously, neurons extend their arbors and form superfluous synapses that are sequentially removed, reorganized, or refined via activity-dependent mechanisms that in turn shape the characteristic hippocampal circuitry.

Most data about the maturation of neuronal pathways has been obtained in anatomical and immunohistochemical studies; however, a number of the features, such as the development of intrinsic firing properties or functional synaptic activity, can only be evaluated by direct electrophysiological recordings in living neurons. Unfortunately, electrophysiological developmental research has evaluated these phenomena independently, without investigating how they shape one another to reach neuronal maturity. Additionally, electrophysiological developmental research is mainly based on experiments with rats. The emergence of genetically engineered mice comes together with modern toolkits for studying intricate molecular developmental mechanisms. Considering this phenomena, developmental electrophysiological profiles in mice will be necessary for further exploration of the developing brain.

The aim of our study was to evaluate synaptic activity and intrinsic firing properties of postnatal hippocampal pyramidal CA1 neurons in mice. To achieve that, we utilized various patch-clamp techniques as well as implemented and optimized a method for preparation, maintenance, and robust electrophysiological recordings in acute mouse brain slices for different ages of postnatal development.

We found substantial developmental changes in the maturation of synaptic activity: the frequency of the recorded synaptic events progressively increased and synaptic transmission was strengthened. Concurrently, hippocampal pyramidal neurons underwent substantial changes in intrinsic firing properties: while input resistance of neuronal membrane decreased, action potentials became higher and shorter, and demonstrated quicker depolarization and repolarization values. More mature pyramidal neurons were better adapted to sustain persistent firing activity. The distinct timelines of these processes indicate that intrinsic firing properties and synaptic activity might affect one another during postnatal development, and more research should be done to investigate this relationship.

The present study described the developmental changes in electrophysiological profiles of hippocampal pyramidal neurons in mice, providing a useful baseline for research with transgenic mice in order to identify specific molecular mechanisms underlying healthy and faulty postnatal development of the brain.

VILNIAUS UNIVERSITETAS

GYVYBĖS MOKSLŲ CENTRAS

BIOMOKSLŲ INSTITUTAS

Kornelija Vitkutė

Magistro baigiamasis darbas

VIDINĖS NEURONO SAVYBĖS IR SINAPSINIS AKTYVUMAS HIPOKAMPO PIRAMIDINIUOSE NEURONUOSE POSTNATALINIO VYSTYMOSI METU

SANTRAUKA

Postnatalinis vystymasis yra kritinis hipokampo piramidinių neuronų vystymuisi ir neuroninių tinklų formavimuisi. Šiuo laikotarpiu nebrandžių piramidinių neuronų membranos plotas smarkiai išauga, o membranoje esančių joninių kanalų skaičius, sudėtis bei kinetinės savybės smarkiai persitvarko. Tai lemia tolygų neuronų spontaninio aktyvumo pasikeitimą į neurono tipui charakteringą neuroninį aktyvumą. Tuo pat metu piramidinių neuronų dendritinės ataugos smarkiai šakojasi ir sudaro gausybę naujų sinapsinių kontaktų. Šis sinapsių perteklius yra pašalinamas ar pertvarkomas nuo aktyvumo priklausomais mechanizmais taip formuojant tipinius hipokampo neuroninius tinklus.

Daug žinių apie neuroninių kelių vystymąsi surinkta anatominių bei imunohistocheminių tyrimų metu, tačiau daug tinklo ypatybių, tokių kaip vidinės neurono savybės ar funkcinis sinapsinis aktyvumas, gali būti įvertinta tik elektrofiziologiniais tyrimais gyvuose neuronuose. Deja, dauguma elektrofiziologinių vystymosi tyrimų atlikti su žiurkėmis. Nauji pelių genetinės modifikacijos metodai suteikia galimybę detaliai tyrinėti su vystymusi susijusius molekulinius mechanizmus. Dėl to natūralu, jog elektrofiziologiniai pelių vystymosi profiliai bus būtini tolimesniems smegenų brandos tyrimams.

Šio tyrimo tikslas buvo įvertinti sinapsinį aktyvumą bei vidines neurono savybes postnataliniu vystymosi periodu pelių hipokampo CA1 piramidiniuose neuronuose. Šiam tikslui pasiekti mes naudojome įvairias *patch-clamp* technikas bei įdiegėme ir optimizavome metodą, tinkamą įvairaus postnatalinio amžiaus ūmių smegenų pjūviams paruošti, palaikyti bei registruoti.

Šio tyrimo metu atskleidėme žymius sinapsinio aktyvumo pakitimus vystymosi metu: sinapsinių įvykių dažnis tolygiai didėjo, o sinapsinis perdavimas sustiprėjo. Tuo pat metu hipokampo piramidiniai neuronų vidinės savybės reikšmingai keitėsi: membranos įėjimo varža smarkiai sumažėjo, veikimo potencialai tapo aukštesni bei trumpesni bei demonstravo greitesnę depoliarizaciją ir repoliarizaciją. Brandesni piramidiniai neuronai buvo geriau prisitaikę palaikyti didesnį veikimo potencialų dažnį.

Skirtingi šių procesų kitimai laike indikuoja, jog vidinės neurono savybės ir sinapsinis aktyvumas galimai įtakoja vienas kitą postnatalinio vystymosi metu; todėl daugiau tyrimų turėtų tikslingai įvertinti šias galimas sąsajas.

Šiame tyrime aprašyti hipokampo piramidinių neuronų elektrofiziologiniai profiliai postnatalinio vystymosi metu bus naudingi tolimesniems tyrimams su transgeninėmis pelėmis, norint atskleisti specifinius molekulinius mechanizmus, susijusius su sveiku ar sutrikusiu postnataliniu smegenų brendimu.

REFERENCES

(87 references total)

Altman J, Bayer SA. Migration and Distribution of Two Populations of Hippocampal Granule Cell PrecursorsDurrng the Perinatal and Postnatal Periods. J Comp Neurol 1990;301:365–81.

Amaral DG, Dent JA. Development of the mossy fibers of the dentate gyrus: I. A light and electron microscopic study of the mossy fibers and their expansions. J Comp Neurol 1981;195:51–86. doi:10.1002/cne.901950106.

Amaral DG, Witter MP. The three-dimensional organization of the hippocampal formation: a review of anatomical data. Neuroscience 1989;31:571–91. doi:10.1159/000257527.

Angevine JB. Time of neuron origin in the hippocampal region. Exp Neurol 1965;11:1–39. doi:10.1016/0014-4886(65)90121-4.

Atwood HL, Wojtowicz JM. Silent Synapses in Neural Plasticity: Current Evidence. Learn Mem 1999:542–71.

Barbin G, Pollard H, Gaïarsa JL, Ben-Ari Y. Involvement of GABAA receptors in the outgrowth of cultured hippocampal neurons. Neurosci Lett 1993;152:150–4. doi:10.1016/0304-3940(93)90505-F.

Ben-Ari Y. Excitatory actions of GABA during development: The nature of the nurture. Nat Rev Neurosci 2002;3:728–39. doi:10.1038/nrn920.

Ben-Ari Y, Cherubini E, Corradetti R, Gaiarsa JL. Giant synaptic potentials in immature rat CA3 hippocampal neurones. J Physiol 1989;416:303–25. doi:10.1113/jphysiol.1989.sp017762.

Bienkowski MS, Bowman I, Song MY, Gou L, Ard T, Cotter K, et al. Integration of gene expression and brain-wide connectivity reveals the multiscale organization of mouse hippocampal networks. Nat Neurosci 2018;21:1628–43. doi:10.1038/s41593-018-0241-y.

Blankenship AG, Feller MB. Mechanisms underlying spontaneous patterned activity in developing neural circuits. Nat Rev Neurosci 2010;11:18–29. doi:10.1038/nrn2759.

Bliss TVP, Lomo T. LONG-LASTING POTENTIATION OF SYNAPTIC TRANSMISSION IN THE DENTATE AREA OF THE ANAESTHETIZED RABBIT FOLLOWING STIMULATION OF THE PERFORANT PATH. J Physiol 1973;232:331–56. doi:10.1113/jphysiol.1973.sp010273.

Choi S, Klingauf J, Tsien RW. Postfusional regulation of cleft glutamate concentration during LTP at "silent synapses." Nat Neurosci 2000;3:330–6. doi:10.1038/73895.

Christophe E, Doerflinger N, Lavery DJ, Molnár Z, Charpak S, Audinat E. Two populations of layer V pyramidal cells of the mouse neocortex: Development and sensitivity to anesthetics. J Neurophysiol 2005;94:3357–67. doi:10.1152/jn.00076.2005.

Couraud F, Martin-Moutot N, Koulakoff A, Berwald-Netter Y. Neurotoxin-sensitive sodium channels in neurons developing in vivo and in vitro. J Neurosci 1986;6:192–8. doi:10.1523/jneurosci.06-01-00192.1986.

Durand GM, Kovalchuk Y, Konnerth A. Long-term potentiation and functional synapse induction in developing hippocampus. Nature 1996:71–5.

Falk T, Kilani RK, Strazdas LA, Borders RS, Steidl J V., Yool AJ, et al. Developmental regulation of the A-type potassium-channel current in hippocampal neurons: Role of the Kvβ1.1 subunit. Neuroscience 2003;120:387–404. doi:10.1016/S0306-4522(03)00044-7.

Fanselow MS, Dong HW. Are the Dorsal and Ventral Hippocampus Functionally Distinct Structures? Neuron 2010;65:7–19. doi:10.1016/j.neuron.2009.11.031.

Feng Y, Weijdegård B, Wang T, Egecioglu E, Fernandez-Rodriguez J, Huhtaniemi I, et al. Spatiotemporal expression of androgen receptors in the female rat brain during the oestrous cycle and the impact of exogenous androgen administration: A comparison with gonadally intact males. Mol Cell Endocrinol 2010;321:161–74. doi:10.1016/j.mce.2010.02.029.

Garaschuk O, Hanse E, Konnerth A. Developmental profile and synaptic origin of early network oscillations in the CA1 region of rat neonatal hippocampus. J Physiol 1998;507:219–36. doi:10.1111/j.1469-7793.1998.219bu.x.

Geinisman Y, Berry RW, Disterhoft JF, Power JM, Van Der Zee EA. Associative learning elicits the formation of multiple-synapse boutons. J Neurosci 2001;21:5568–73. doi:10.1523/jneurosci.21-15-05568.2001.

Gould E., Westlind-Danielsson A, Frankfurt M, McEwen BS. Sex differences and thyroid hormone sensitivity of hippocampal pyramidal cells. J Neurosci 1990;10:996–1003. doi:10.1523/jneurosci.10-03-00996.1990.

Gould Elizabeth, Woolley CS, Frankfurt M, McEwen BS. Gonadal steroids regulate dendritic spine density in hippocampal pyramidal cells in adulthood. J Neurosci 1990;10:1286–91. doi:10.1523/jneurosci.10-04-01286.1990.

Groc L, Gustafsson B, Hanse E. Spontaneous unitary synaptic activity in CA1 pyramidal neurons during early postnatal development: constant contribution of AMPA and NMDA receptors. J Neurosci 2002;22:5552–62. doi:20026547.

Guan D, Horton LR, Armstrong WE, Foehring RC. Postnatal development of A-type and Kv1- and Kv2-mediated potassium channel currents in neocortical pyramidal neurons. J Neurophysiol 2011;105:2976–88. doi:10.1152/jn.00758.2010.

Guan D, Lee JCF, Higgs MH, Spain WJ, Foehring RC. Functional roles of Kv1 channels in neocortical pyramidal neurons. J Neurophysiol 2007;97:1931–40. doi:10.1152/jn.00933.2006.

Harris,' KM, Jensen,' FE, Tsao' B. Three-Dimensional Structure of Dendritic Spines and Synapses in Rat Hippocampus (CAI) at Postnatal Day 15 and Adult Ages: Implications for the Maturation of Synaptic Physiology and Long-term Potentiation. vol. 12. 1992.

Hayashi K, Kubo KI, Kitazawa A, Nakajima K. Cellular dynamics of neuronal migration in the hippocampus. Front Neurosci 2015;9:135. doi:10.3389/fnins.2015.00135.

He L, Xue L, Xu J, McNeil BD, Bai L, Melicoff E, et al. Compound vesicle fusion increases quantal size and potentiates synaptic transmission. Nature 2009;459:93–7. doi:10.1038/nature07860.

Hondeghem LM. Validity of Vmax as a measure of the sodium current in cardiac and nervous tissues. Biophys J 1978;23:147–52. doi:10.1016/S0006-3495(78)85439-3.

Hsia Albert Y., Malenka RC, Nicoll RA. Development of excitatory circuitry in the hippocampus. J Neurophysiol 1998;79:2013–24. doi:10.1152/jn.1998.79.4.2013.

Hsia Albert Y, Malenka RC, Nicoll RA, Albert Y, Malenka RC, De- RAN. Development of Excitatory Circuitry in the Hippocampus. J Neurophysiol 1998;79:2013–24.

Huttenlocher PR, Dabholkar AS. Regional Differences in Synaptogenesis in Human Cerebral Cortex. J Comp Neurol 1997;178:167–78.

Isaac JTR, Nicoll RA, Malenka RC. Evidence for silent synapses: Implications for the expression of LTP. Neuron 1995;15:427–34. doi:10.1016/0896-6273(95)90046-2.

Johnson-Venkatesh EM, Khan MN, Murphy GG, Sutton MA, Umemori H. Excitability governs neural development in a hippocampal region-specific manner. Development 2015:3879–91. doi:10.1242/dev.121202.

Juraska JM, Fitch JM, Washburne DL. The dendritic morphology of pyramidal neurons in the rat hippocampal CA3 area. II. Effects of gender and the environment. Brain Res 1989;479:115–9. doi:10.1016/0006-8993(89)91341-3.

Katz LC, Shatz CJ. Synaptic Activity and the Construction of Cortical Circuits. Science (80-) 1996;274:1133–8. doi:10.1126/science.274.5290.1133.

Kerchner GA, Nicoll RA. Silent synapses and the emergence of a postsynaptic mechanism for LTP. Nat Rev Neurosci 2008;9:813–25. doi:10.1038/nrn2501.

Lanore F, Labrousse VF, Szabo Z, Normand E, Blanchet C, Mulle C. Deficits in morphofunctional maturation of hippocampal mossy fiber synapses in a mouse model of intellectual disability. J Neurosci 2012;32:17882–93. doi:10.1523/JNEUROSCI.2049-12.2012.

Leinekugel X, Medina I, Khalilov I, Ben Ari Y, Khazipov R. Ca 2 ¼ Oscillations Mediated by the Synergistic Excitatory Actions of GABA. Neuron 1997;18:243–55.

Lenz KM, Nugent BM, Haliyur R, McCarthy MM. Microglia Are Essential to Masculinization of Brain and Behavior. J Neurosci 2013;33:2761–72. doi:10.1523/jneurosci.1268-12.2013.

Liao D, Hessler NA, Mallnow R. Activation of postsynaptically silent synapses during pairing-induced LTP in CA1 region of hippocampal slice. Nature 1995;375:400–4.

Liu PW, Bean BP. Kv2 channel regulation of action potential repolarization and firing patterns in superior cervical ganglion neurons and hippocampal CA1 pyramidal neurons. J Neurosci 2014;34:4786–800. doi:10.1523/JNEUROSCI.1925-13.2014.

Lømo T. Frequency potentiation of excitatory synaptic activity in the dentate area of the hippocampal formation. Acta Physiol Scand 1966. doi:citeulike-article-id:3133405.

Lorenzon NM, Foehring RC. The ontogeny of repetitive firing and its modulation by norepinephrine in rat neocortical neurons. Dev Brain Res 1993;73:213–23. doi:10.1016/0165-3806(93)90141-V.

Marchal C, Mulle C. Postnatal maturation of mossy fibre excitatory transmission in mouse CA3 pyramidal cells: a potential role for kainate receptors. J Physiol 2004;561:27–37. doi:10.1113/jphysiol.2004.069922.

Mccormick BYDA, Prince DA. Postnatal development of electrophysiological properties of rat cerebral cortical pyramidal neurons. J Physiol 1987;393:743–62.

McCormick DA, Prince DA. Post-natal development of electrophysiological properties of rat cerebral cortical pyramidal neurones. J Physiol 1987;393:743–62. doi:10.1113/jphysiol.1987.sp016851.

McGrath, Saha, Welham, El-Saadi, MacCauley, Chant. A systematic review of the incidence of schizophrenia: The distribution of rate items and the influence of methodology, urbanicity, sex and migrant status. Schizophr Res 2004;67:65–6.

Michelson HB, Lothman EW. An in vivo electrophysiological study of the ontogeny of excitatory and inhibitory processes in the rat hippocampus. Dev Brain Res 1989;47:113–22. doi:10.1016/0165-3806(89)90113-2.

Miyamoto A, Wake H, Ishikawa AW, Eto K, Shibata K, Murakoshi H, et al. Microglia contact induces synapse formation in developing somatosensory cortex. Nat Commun 2016;7:1–12. doi:10.1038/ncomms12540.

Mogi K, Takanashi H, Nagasawa M, Kikusui T. Sex differences in spatiotemporal expression of AR,

ERα, and ERβ mRNA in the perinatal mouse brain. Neurosci Lett 2015;584:88–92. doi:10.1016/j.neulet.2014.10.028.

Monfort P, Gomez-Gimenez B, Llansola M, Felipo V. Gender Differences in Spatial Learning, Synaptic Activity, and Long-Term Potentiation in the Hippocampus in Rats: Molecular Mechanisms. ACS Chem Neurosci 2015;6:1420–7. doi:10.1021/acschemneuro.5b00096.

Moody WJ, Bosma MM. Ion channel development, spontaneous activity, and activity-dependent development in nerve and muscle cells. Physiol Rev 2005;85:883–941. doi:10.1152/physrev.00017.2004.

Nelson LH, Warden S, Lenz KM. Sex differences in microglial phagocytosis in the neonatal hippocampus. Brain Behav Immun 2017;64:11–22. doi:10.1016/j.bbi.2017.03.010.

Neniskyte U, Gross CT. Errant gardeners: Glial-cell-dependent synaptic pruning and neurodevelopmental disorders. Nat Rev Neurosci 2017;18:658–70. doi:10.1038/nrn.2017.110.

Oswald AMM, Reyes AD. Maturation of intrinsic and synaptic properties of layer 2/3 pyramidal neurons in mouse auditory cortex. J Neurophysiol 2008;99:2998–3008. doi:10.1152/jn.01160.2007.

Paolicelli RC, Bolasco G, Pagani F, Maggi L, Scianni M, Panzanelli P, et al. Synaptic pruning by microglia is necessary for normal brain development. Science (80-) 2011;333:1456–8. doi:10.1126/science.1202529.

Parkhurst CN, Yang G, Ninan I, Savas JN, Yates JR, Lafaille JJ, et al. Microglia promote learning-dependent synapse formation through brain-derived neurotrophic factor. Cell 2013;155:1596–609. doi:10.1016/j.cell.2013.11.030.

Penzes P, Cahill ME, Jones KA, Vanleeuwen JE, Woolfrey KM. Dendritic spine pathology in neuropsychiatric disorders. Nat Neurosci 2011;14:285–93. doi:10.1038/nn.2741.

Pickard L, Noël J, Henley JM, Collingridge GL, Molnar E. Developmental changes in synaptic AMPA and NMDA receptor distribution and AMPA receptor subunit composition in living hippocampal neurons. J Neurosci 2000;20:7922–31.

Picken Bahrey HL, Moody WJ. Early development of voltage-gated ion currents and firing properties in neurons of the mouse cerebral cortex. J Neurophysiol 2003;89:1761–73. doi:10.1152/jn.00972.2002.

Qi X, Zhang K, Xu T, Yamaki VN, Wei Z, Huang M, et al. Sex differences in long-term potentiation at temporoammonic-CA1 synapses: Potential implications for memory consolidation. PLoS One 2016;11:1–18. doi:10.1371/journal.pone.0165891.

Richards DA, Mateos JM, Hugel S, De Paola V, Caroni P, Gähwiler BH, et al. Glutamate induces the rapid formation of spine head protrusions in hippocampal slice cultures. Proc Natl Acad Sci U S A 2005;102:6166–71. doi:10.1073/pnas.0501881102.

Routh BN, Johnston D, Harris K, Chitwood RA. Anatomical and electrophysiological comparison of CA1 pyramidal neurons of the rat and mouse. J Neurophysiol 2009;102:2288–302. doi:10.1152/jn.00082.2009.

Salter EW, Sunstrum JK, Matovic S, Inoue W. Chronic stress dampens excitatory synaptic gain in the paraventricular nucleus of the hypothalamus. J Physiol 2018;596:4157–72. doi:10.1113/JP275669.

Sánchez-Alonso JL, Sánchez-Aguilera A, Vicente-Torres MA, Colino A. Intrinsic excitability is altered by hypothyroidism in the developing hippocampal CA1 pyramidal cells. Neuroscience 2012;207:37–51. doi:10.1016/j.neuroscience.2012.01.030.

Schafer DP, Lehrman EK, Kautzman AG, Koyama R, Mardinly AR, Yamasaki R, et al. Microglia Sculpt Postnatal Neural Circuits in an Activity and Complement-Dependent Manner. Neuron 2012;74:691–

705. doi:10.1016/j.neuron.2012.03.026.

Schwartzkroin PA. Development of rabbit hippocampus: Physiology. Dev Brain Res 1981;2:469–86. doi:10.1016/0165-3806(81)90017-1.

Schwarz JM, Sholar PW, Bilbo SD. Sex differences in microglial colonization of the developing rat brain. J Neurochem 2012;120:948–63. doi:10.1111/j.1471-4159.2011.07630.x.

Sekar A, Bialas AR, De Rivera H, Davis A, Hammond TR, Kamitaki N, et al. Schizophrenia risk from complex variation of complement component 4. Nature 2016;530:177–83. doi:10.1038/nature16549.

Sipe GO, Lowery RL, Tremblay M, Kelly EA, Lamantia CE, Majewska AK. Microglial P2Y12 is necessary for synaptic plasticity in mouse visual cortex. Nat Commun 2016;7. doi:10.1038/ncomms10905.

Spigelman I, Zhang L, Carlen PL. Patch-clamp study of postnatal development of CA1 neurons in rat hippocampal slices: membrane excitability and K+ currents. J Neurophysiol 1992;68:55–69. doi:10.1152/jn.1992.68.1.55.

Spigelman I., Zhang L, Carlen PL. Patch-clamp study of postnatal development of CA1 neurons in rat hippocampal slices: Membrane excitability and K+ currents. J Neurophysiol 1992;68:55–69. doi:10.1152/jn.1992.68.1.55.

Steward O, Falk PM. Selective localization of polyribosomes beneath developing synapses: A quantitative analysis of the relationships between polyribosomes and developing synapses in the hippocampus and dentate gyrus. J Comp Neurol 1991;314:545–57. doi:10.1002/cne.903140311.

Strichartz G, Cohen I. Vmax as a measure of GNa in nerve and cardiac membranes. Biophys J 1978;23:153–6. doi:10.1016/S0006-3495(78)85440-X.

Ting JT, Lee BR, Chong P, Soler-Llavina G, Cobbs C, Koch C, et al. Preparation of Acute Brain Slices Using an Optimized N-Methyl-D-glucamine Protective Recovery Method. J Vis Exp 2018. doi:10.3791/53825.

Tsai NP, Wilkerson JR, Guo W, Maksimova MA, Demartino GN, Cowan CW, et al. Multiple autism-linked genes mediate synapse elimination via proteasomal degradation of a synaptic scaffold PSD-95. Cell 2012;151:1581–94. doi:10.1016/j.cell.2012.11.040.

Warren SG, Humphreys AG, Juraska JM, Greenough WT. LTP varies across the estrous cycle: enhanced synaptic plasticity in proestrus rats. Brain Res 1995;703:26–30. doi:10.1016/0006-8993(95)01059-9.

Weinhard L, Di Bartolomei G, Bolasco G, Machado P, Schieber NL, Neniskyte U, et al. Microglia remodel synapses by presynaptic trogocytosis and spine head filopodia induction. Nat Commun 2018a;9. doi:10.1038/s41467-018-03566-5.

Weinhard L, Neniskyte U, Vadisiute A, di Bartolomei G, Aygün N, Riviere L, et al. Sexual dimorphism of microglia and synapses during mouse postnatal development. Dev Neurobiol 2018b;78:618–26. doi:10.1002/dneu.22568.

Werling DM, Geschwind DH. Sex differences in autism spectrum disorders. Curr Opin Neurol 2013;26:146–53. doi:10.1097/WCO.0b013e32835ee548.

Werling DM, Parikshak NN, Geschwind DH. Gene expression in human brain implicates sexually dimorphic pathways in autism spectrum disorders. Nat Commun 2016;7:1–11. doi:10.1038/ncomms10717.

Xiong G, Metheny H, Johnson BN, Cohen AS. A Comparison of Different Slicing Planes in Preservation of Major Hippocampal Pathway Fibers in the Mouse. Front Neuroanat 2017;11:107. doi:10.3389/fnana.2017.00107.

Yagi S, Galea LAM. Sex differences in hippocampal cognition and neurogenesis. Neuropsychopharmacology 2019;44:200–13. doi:10.1038/s41386-018-0208-4.

Zhan Y, Paolicelli RC, Sforazzini F, Weinhard L, Bolasco G, Pagani F, et al. Deficient neuron-microglia signaling results in impaired functional brain connectivity and social behavior. Nat Neurosci 2014;17:400–6. doi:10.1038/nn.3641.

Zhang JQ, Cai WQ, Zhou DS, Su BY. Distribution and differences of estrogen receptor beta immunoreactivity in the brain of adult male and female rats. Brain Res 2002;935:73–80. doi:10.1016/S0006-8993(02)02460-5.

Zhang ZW. Maturation of Layer V Pyramidal Neurons in the Rat Prefrontal Cortex: Intrinsic Properties and Synaptic Function. J Neurophysiol 2004;91:1171–82. doi:10.1152/jn.00855.2003.

AKNOWLEDGEMENTS

I am deeply grateful for my supervisor **dr. Urtė Neniškytė** for invaluable guidance throughout these past years. The unparalleled support and insightful advice have pushed me to do my best. I could not thank more **prof**. **dr. Aidas Alaburda** for sharing extensive knowledge and experience as well as always being there to aid me with anything I was struggling with during my experiments. This work would be impossible without the guidance of these people.

I kindly thank **dr. Gytis Baranauskas** for sharing his valuable time and experience to advance this research. I would also like to thank all my laboratory peers who supported me and were a joy to work and spend time with. Also, I kindly thank members of the department of Neurobiology and Biophysics, who were always there to teach me, help me and give valuable advice.

SUPPLEMENTARY
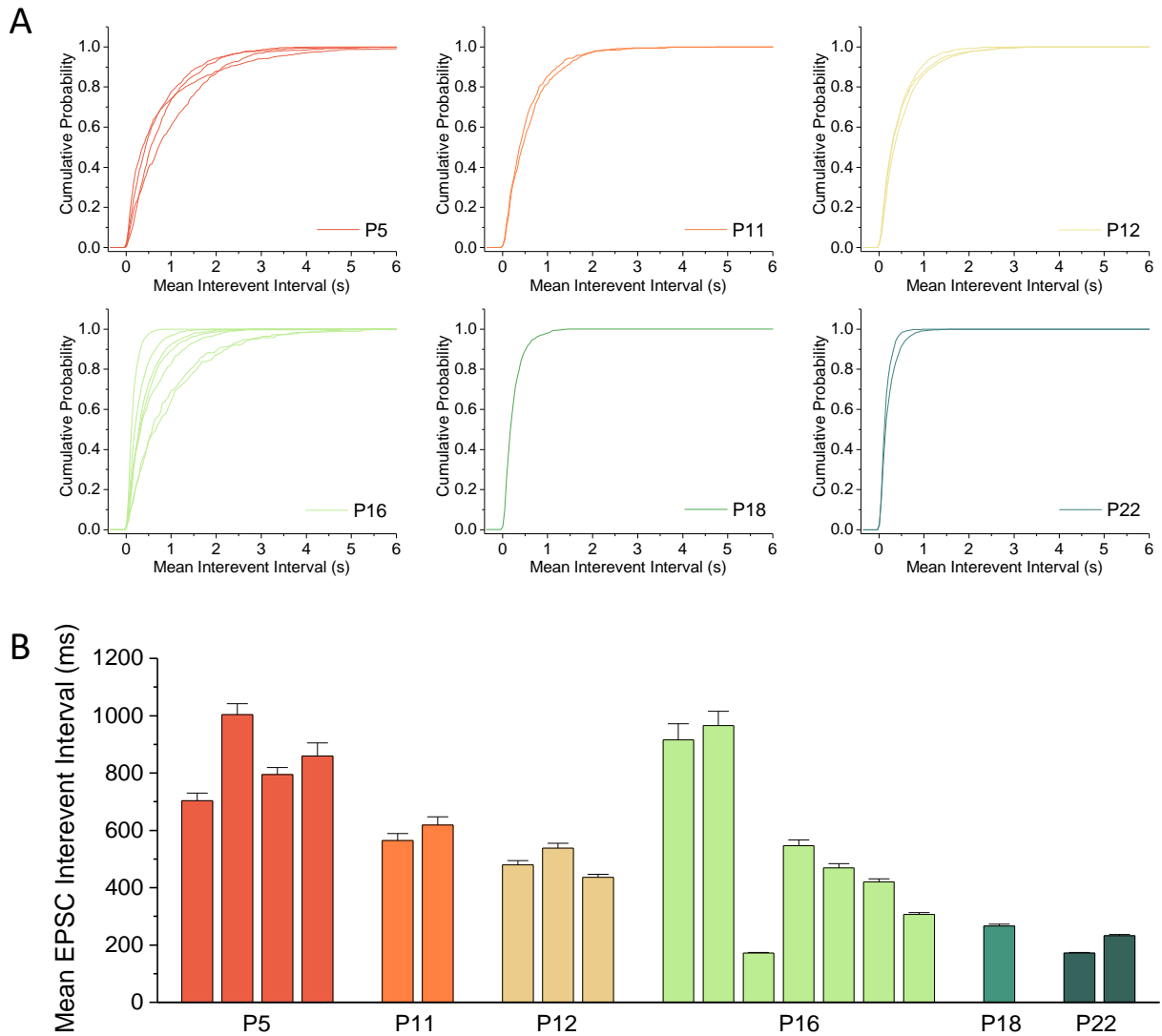
Figure S1 **EPSC Interevent Intervals during postnatal development: individual neuron graphs. *A*** Cumulative probability graphs of EPSC interevent intervals graphed by age and individual neurons: (P5(n=4), red; P11(n=2), orange; P12(n=3), yellow; P16(n=7), green; P18(n=1), dark green; P22(n=2),dark blue); ***B*** Mean EPSC interevent interval durations during postnatal development graphed by age and individual neuron values. Data are presented as a mean $\pm$ SEM;
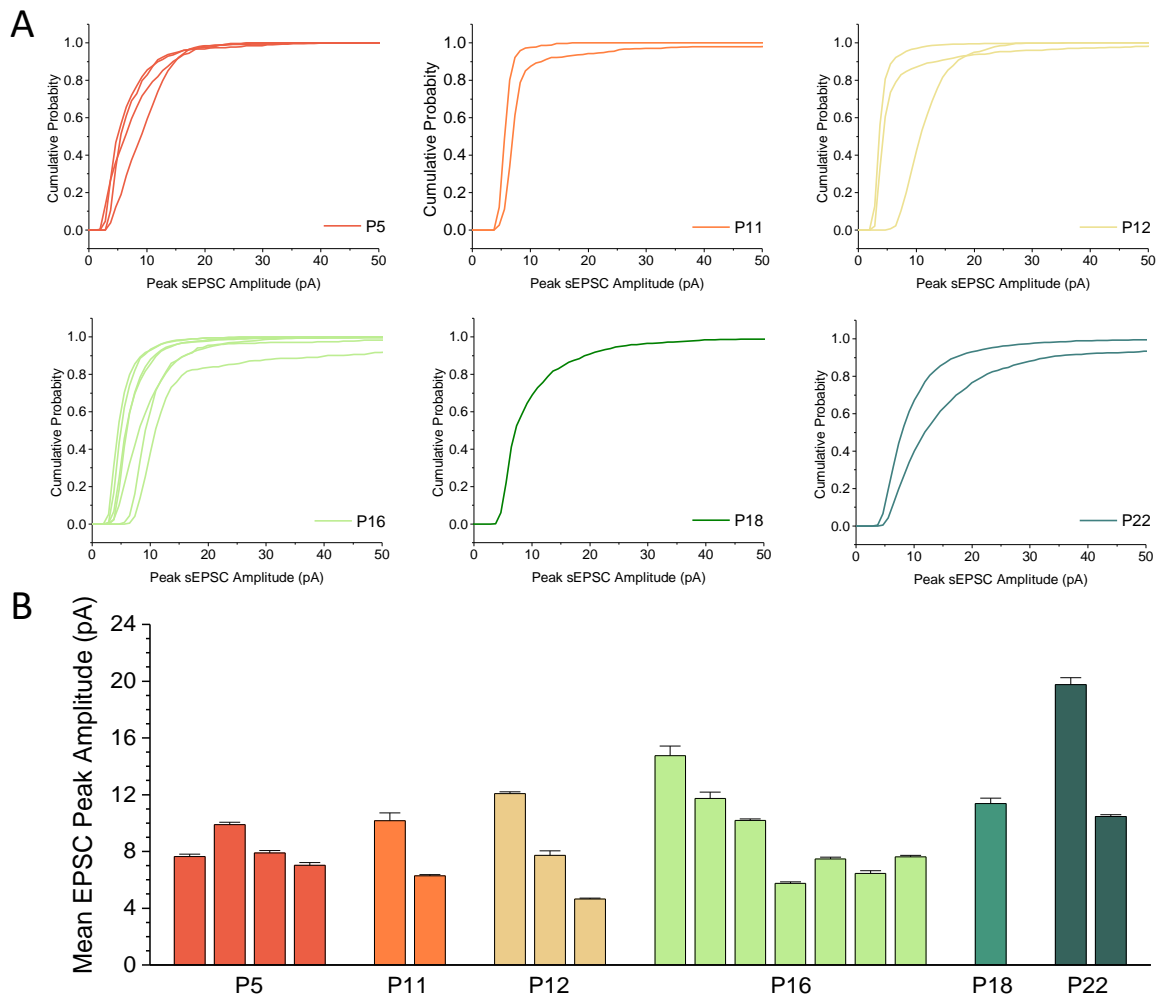
Figure S2 **Peak EPSC Amplitudes during postnatal development: individual neuron graphs. *A*** Cumulative probability graphs of Peak EPSC amplitudes graphed by age and individual neurons: (P5(n=4), red; P11(n=2), orange; P12(n=3), yellow; P16(n=7), green; P18(n=1), dark green; P22(n=2),dark blue); ***B*** Mean peak EPSC amplitudes during postnatal development graphed by age and individual neuron values. Data are presented as a mean $\pm$ SEM;
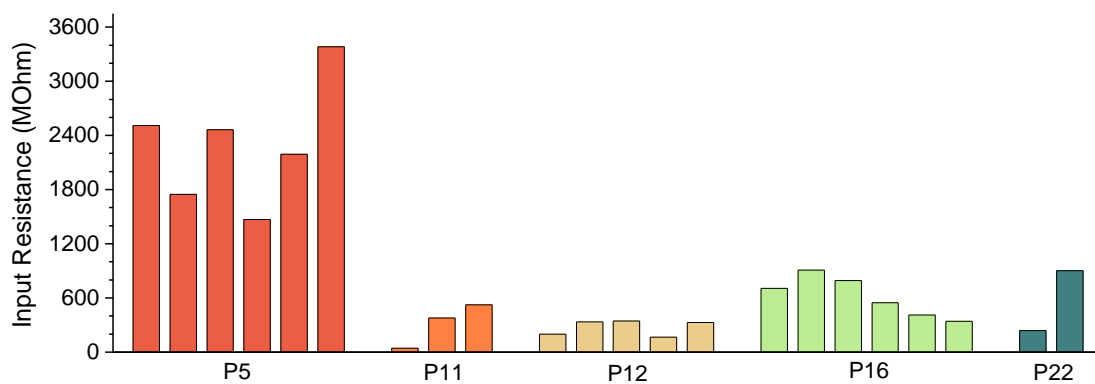

Figure S3 **Input Resistance during postnatal development.** Input resistance values of individual neurons during postnatal development.
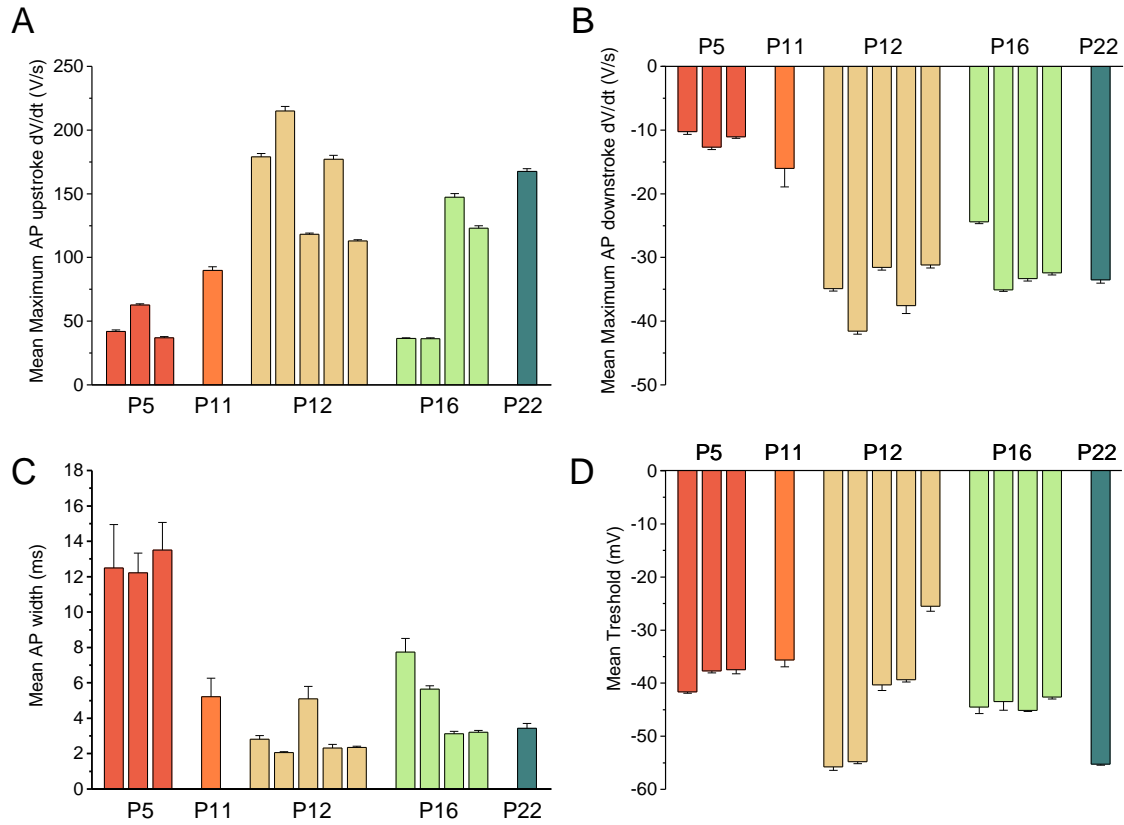
Figure S4 **Action potential characteristics during development: individual neuron graphs. *A*** Maximum action potential upstroke derivative values of individual neurons during postnatal development. ***B*** Maximum action potential downstroke derivative values of individual neurons during postnatal development. ***C*** Mean action potential width during postnatal development ***D*** Mean action potential threshold during postnatal development. Number of neurons analyzed in A, B, C and D: P5(n=3); P11(n=1); P12(n=5); P16(n=4); P22 (n=1). Data in A, B, C and D are presented as a mean ± SEM;
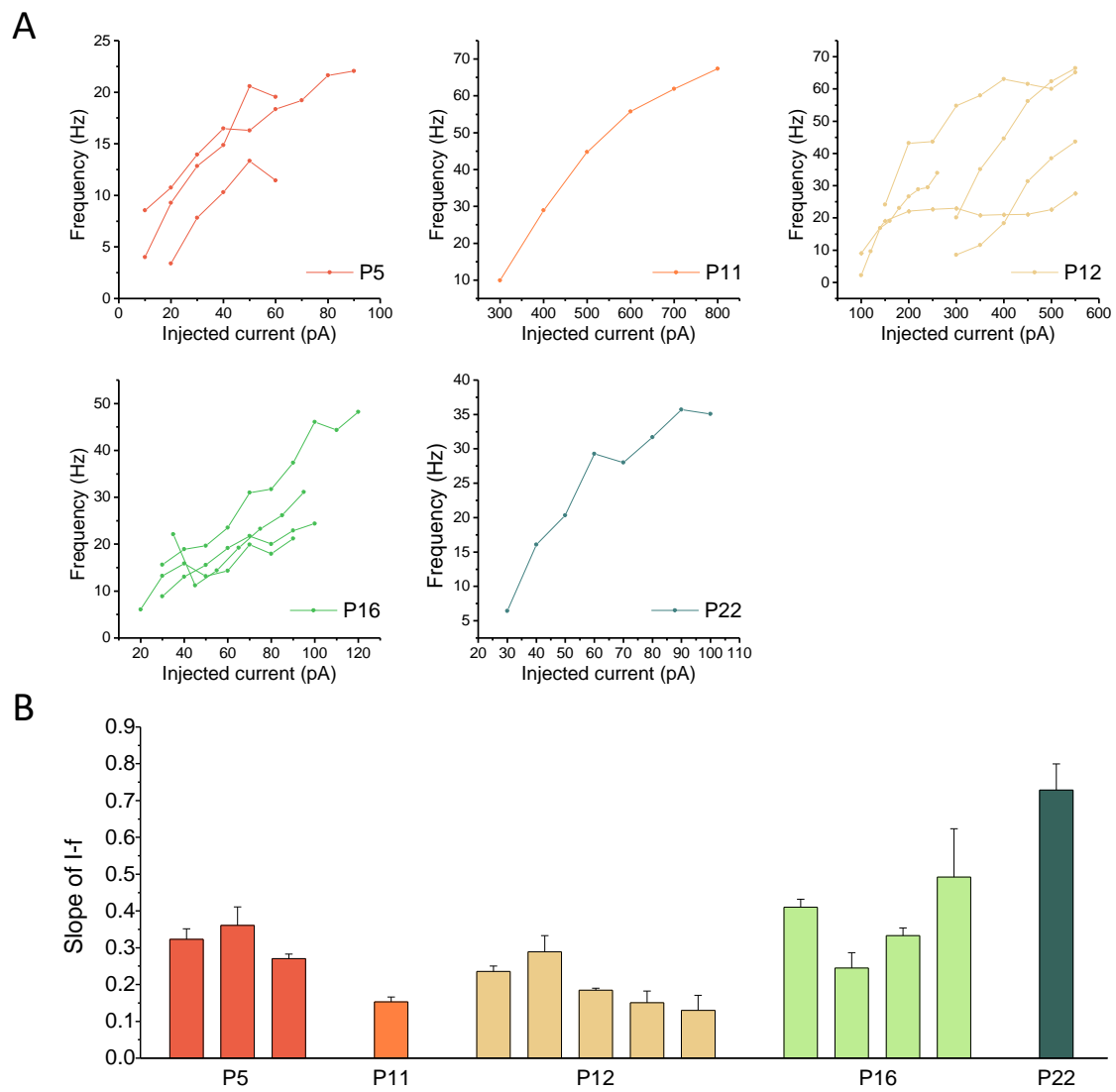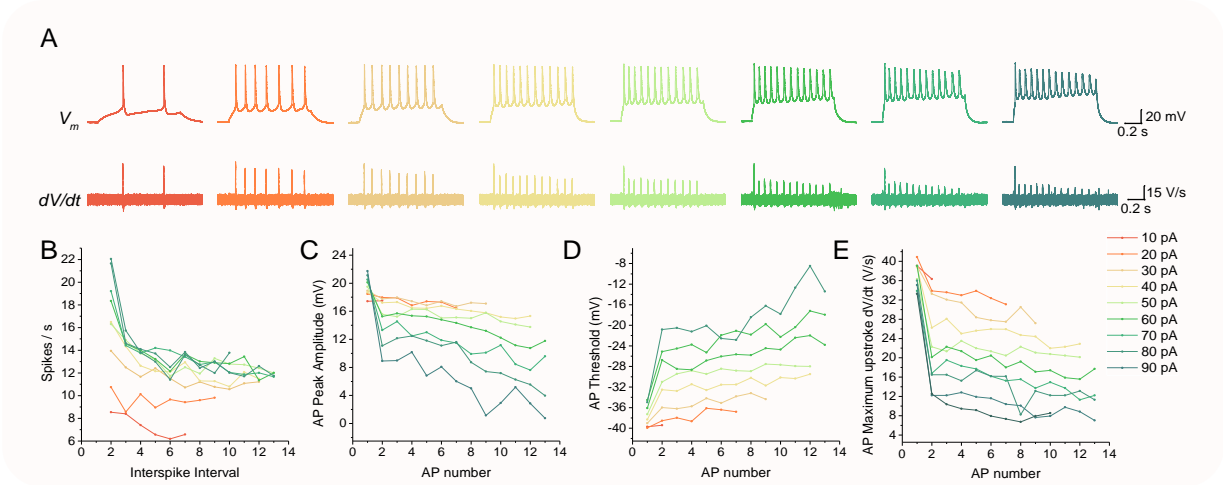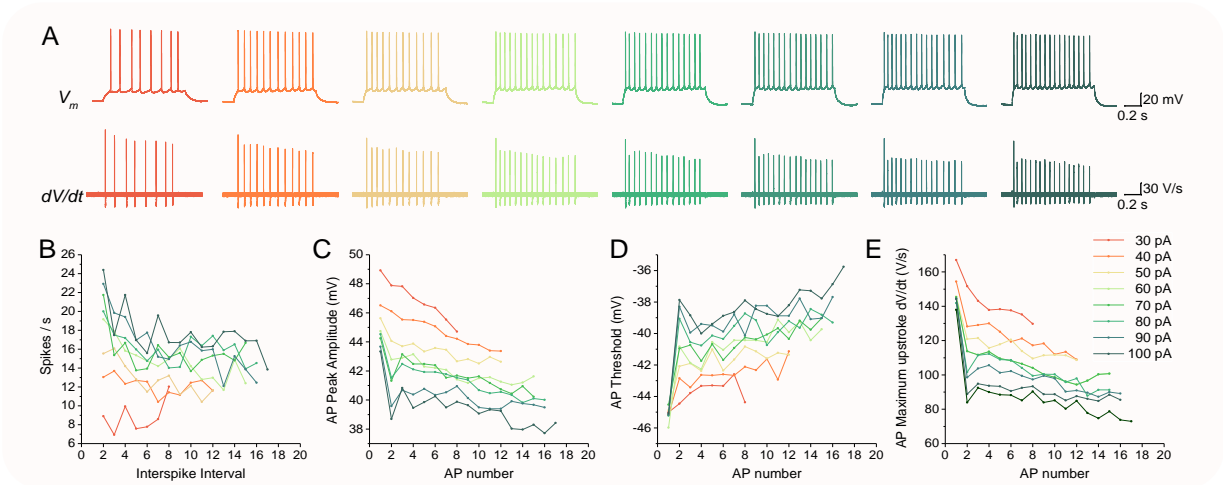
Figure S5 **f-I relations and gain during postnatal development: individual neuron graphs. A** Transfer functions (f-I relationships) graphed by individual neurons and grouped by age **B** Mean gains (the slope of the linear fit of the f-I curve) of individual neurons during postnatal development. Data are presented as a mean ± SEM;
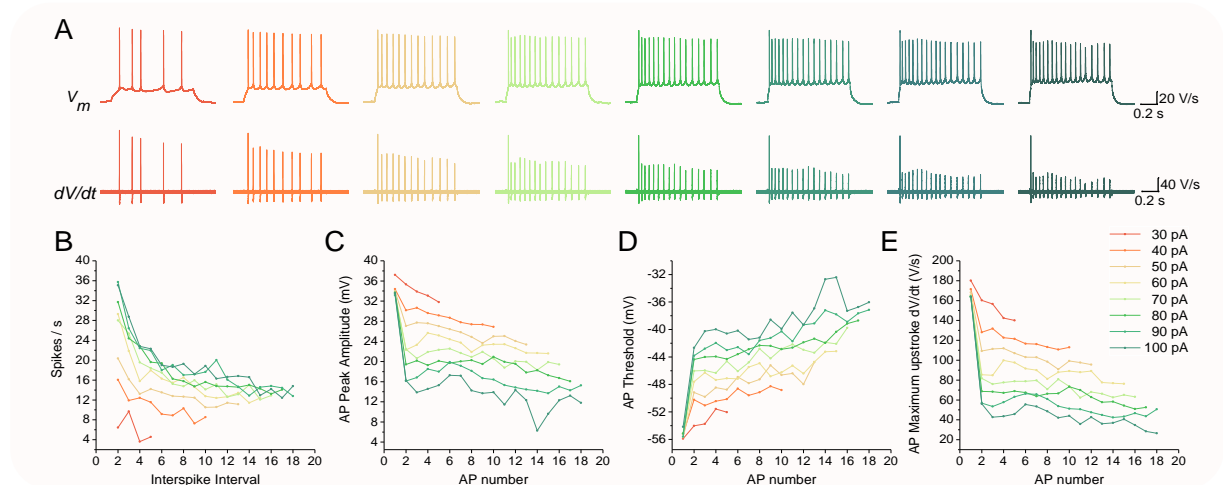
Figure S6 **Developmental profiles of intrinsic firing properties.** Representative developmental profiles of intrinsic firing properties at P5, P16 and P22. *A* Voltage traces of every recorded sweep in response to a second-long square waveform current. The injected current value was increased with each sweep. (10 pA increments); Red: lowest injected current; Dark blue: largest injected current; *B* Firing rate values for every interspike interval in every sweep. *C* Action potential peaks for every action potential in every sweep. *D* Action potential threshold values for every action potential in every sweep. *E* Action potential maximum upstroke derivatives for every action potential in every sweep.